Published in final edited form as:

Nature. 2019 July ; 571(7765): 424–428. doi:10.1038/s41586-019-1374-1.

m^{6}A enhances the phase separation potential of mRNA

Ryan J. Ries[1], **Sara Zaccara**[1], **Pierre Klein**[1], **Anthony Olarerin-George**[1], **Sim Namkoong**[2], **Brian F. Pickering**[1], **Deepak P. Patil**[1], **Hojoong Kwak**[3], **Jun Hee Lee**[2], **Samie R. Jaffrey**[1]

[1]Department of Pharmacology, Weill-Cornell Medical College, Cornell University, New York, NY 10065, USA

[2]Department of Molecular and Integrative Physiology, University of Michigan, Ann Arbor, MI 48109, USA

[3]Department of Molecular Biology and Genetics, Cornell University, Ithaca, NY 14853, USA

Abstract

N^6-methyladenosine (m^{6}A) is the most prevalent modified nucleotide in mRNA[1,2], with ~25% of mRNAs containing at least one m^{6}A. Methylation of mRNA to form m^{6}A is required for diverse cellular and physiological processes[3]. Although the presence of m^{6}A in an mRNA can affect its fate in different ways, it is unclear how m^{6}A directs this process and why the effects of m^{6}A can vary in different cellular contexts. Here we show that the cytosolic m^{6}A-binding proteins, YTHDF1–3, undergo liquid-liquid phase separation (LLPS) *in vitro* and in cells. This LLPS is markedly enhanced by mRNAs that contain multiple, but not single, m^{6}A residues. Polymethylated mRNAs act as a multivalent scaffold for binding YTHDF proteins, juxtaposing their low-complexity domains, leading to phase separation. The resulting mRNA-YTHDF complexes then partition into different endogenous phase-separated compartments, such as P-bodies, stress granules, or neuronal RNA granules. m^{6}A-mRNA is subject to compartment-specific regulation, including reduced mRNA stability and translation. These studies reveal that the number and distribution of m^{6}A sites in cellular mRNAs can regulate and influence the composition of the phase-separated transcriptome. Additionally, these findings indicate that the cellular properties of m^{6}A-modified mRNAs are governed by liquid-liquid phase separation principles.

Correspondence should be addressed to S.R.J. (srj2003@med.cornell.edu).

Author contributions

S.R.J., R.J.R., A.O.-G., S.Z. and P.K. designed the experiments. R.J.R and P.K. carried out stress granule staining experiments, S.N., J.H.L. and H.K. prepared stress granules, R.J.R. and P.K. performed assays related to phase separation and stress granule formation, P.K. performed puromycin labeling assays, R.J.R. performed quantification of stress granules and smFISH, R.J.R, P.K. and S.Z. analyzed ribosome profiling data, A.O.-G. and R.J.R. performed analysis of stress granule transcriptomes, B.P. performed m^{6}A measurements and D.P.P. made DF expression constructs. S.Z. performed CRISPR knock-in, R.J.R. and S.Z. performed in-cell FRAP experiments. R.J.R. and S.Z. prepared Figures relating to ribosome profiling data. R.J.R., S.Z., and P.K. prepared the remaining Figures. S.R.J. wrote the manuscript with input from all authors.

Competing interests S.R.J. declares a competing interest; he is scientific founder, advisor to, and owns equity in Gotham Therapeutics.

Supplementary Information is linked to the online version of the paper at www.nature.com/nature.

To understand how m^{6}A affects mRNA fate, we considered the biochemical properties of the major cytosolic m^{6}A-binding proteins YTHDF1, YTHDF2, and YTHDF3 (DF1, DF2, and DF3, respectively). These paralogous proteins exhibit high sequence identity and comprise a ~15 kDa YTH domain that binds m^{6}A, and a ~40 kDa low-complexity domain that includes prion-like domains (Extended Data Fig. 1a)[4].

Some low-complexity sequences form fibrils, hydrogels or liquid droplets as a result of phase separation[5,6]. To test whether DF proteins form these condensates, we purified full-length recombinant DF2, the most abundant DF paralog in most cells[4]. DF2 solutions were clear at 4ºC, but became turbid upon warming to 37ºC, and then became clear again after cooling to 4ºC (Fig. 1a). Using phase contrast microscopy, we observed protein droplets that only formed in the warmed samples (Fig. 1b). This warming-induced liquid-liquid phase separation (LLPS) is suggestive of lower critical solution temperature phase separation[7]. This type of phase separation is associated with Pro-X_n-Gly motifs, which are enriched in DF proteins (Extended Data Fig. 1a).

DF2 LLPS is enhanced by increased protein concentration and dampened by salt (Fig. 1c). Adding as little as 10% glycerol and lowering salt concentrations reduced the DF2 concentration required for phase transition to 1 μM–8 μM (Fig. 1c). This concentration is consistent with the ~5 μM intracellular concentration of endogenous DF proteins[8]. Imaging Alexa488-labeled DF2 (Extended Data Fig. 1b) showed droplets fusing to form larger droplets (Fig. 1d, Supplementary Video 1). Photobleaching of a region of an Alexa488-labeled DF2 droplet was associated with rapid recovery of fluorescence (Fig. 1e), consistent with DF2 exhibiting liquid-like properties[9]. DF2 LLPS requires its low-complexity domain, as removal of this domain prevented LLPS, even at high protein concentrations (Extended Data Fig. 1c). Each DF paralog exhibits LLPS (Extended Data Fig. 1d) and mixing all three DF proteins resulted in droplets that contained all three proteins, suggesting that these proteins interact and phase separate together (Extended Data Fig. 1e). Overall, these studies reveal that LLPS is a physical property of the DF proteins, at least *in vitro*.

We asked if m^{6}A-RNA binding to the YTH domain regulates LLPS. We chose a buffer and protein concentration in which LLPS does not occur. Addition of a 65 nt-long RNA containing 0 or 1 m^{6}A did not induce DF2 LLPS (Fig. 1f, Extended Data Fig. 1f). However, an RNA that contained ten m^{6}A nucleotides triggered LLPS within minutes (Fig. 1f, Extended Data 1g, Supplementary Video 2) and increased the partition coefficient of each DF protein (Fig. 1g, Extended Data 1h). These data suggest that polymethylated m^{6}A-RNA provides a scaffold that juxtaposes multiple DF proteins, causing them to undergo LLPS through interactions between their low-complexity domains. The liquid droplets are therefore composed of a DF-RNA coacervate.

DF proteins localize to neuronal RNA granules, P-bodies, and stress granules[4,10,11], each of which is considered to be a phase-separated compartment in the cytosol[4,10,11], raising the possibility that LLPS may govern the localization of these proteins, and potentially m^{6}A-mRNA. To determine if DF proteins phase separate in cells, we first examined stress granules since they can be induced by various stimuli in a temporally controlled manner. Diverse stimuli, including heat shock, sodium arsenite, and ER stress caused all three DF

proteins to relocalize from throughout the cytosol to stress granules in a range of cell types (Figures 2a–b, Extended Data Fig. 2a–f).

To address if DF2 exhibits liquid-like properties *in vivo*, we used CRISPR/Cas9 to insert NeonGreen into the HEK293 genomic *YTHDF2* locus resulting in endogenous expression of DF2-NeonGreen (Extended Data Fig. 2g). Photobleaching of sodium arsenite-induced stress granules showed rapid recovery of DF2-NeonGreen fluorescence (Fig. 2c, Extended Data Fig. 2h), consistent with the liquid-like *in vitro* behavior of DF2.

In non-stressed cells, DF2 is localized to P-bodies[12]. However, after heat shock stress, we noticed that P-bodies lacked DF2, and were instead adjacent to DF2-labeled granules (Fig. 2d). This suggests that DF2 can partition into different structures: P-bodies in unstressed cells, and to stress granules during stress.

Although previous studies detected a marked increase in DF2 and nuclear relocalization 2 h after heat shock[13], we detected minimal change in DF2 levels and localization exclusively to cytosolic stress granules (Extended Data Fig. 2i). Nevertheless, to determine if DF2 LLPS is due to increased DF2 expression we used translation inhibitors. These did not prevent stress-induced relocalization of DF2 to stress granules (Extended Data Fig. 2j).

We also considered the possibility that stress increases m^{6}A levels in mRNAs. Heat shock and arsenite can increase mRNA methylation when assayed up to 6 hr after cell stress[13–16]. Although our assays were performed immediately after stress, we asked whether increased m^{6}A formation mediates LLPS. Since m^{6}A formation occurs co-transcriptionally[17,18], we blocked m^{6}A formation with the transcription inhibitor actinomycin D. However, transcription inhibition did not reduce DF2 localization to stress granules (Extended Data Fig. 2j). Additionally, m^{6}A levels in cellular poly(A) mRNA did not change after stress (Extended Data Fig. 2k–l). Overall, no new DF2 protein or new mRNA methylation is needed for DF2 to partition into stress granules. Instead, the existing m^{6}A distribution in mRNA at the onset of stress is sufficient to guide DF-m^{6}A-mRNA LLPS.

Nearly all m^{6}A formation in mRNA is catalyzed by the METTL3-METTL14 heterodimeric methyltransferase[19–22]. m^{6}A is not needed for stress granule formation, as stress granule formation appeared largely normal in *Mettl14* knockout mES cells (Fig. 3a, Extended Data Fig. 3a,b). However, DF2 relocalization to stress granules was markedly reduced in *Mettl14* knockout cells (Fig. 3a,b, Extended data Fig. 3b). Similarly, a DF2 mutant that does not bind m^{6}A shows reduced relocalization to stress granules in wild-type cells (Fig. 3c). Thus, DF2 must bind m^{6}A-mRNA to efficiently partition into stress granules.

We also examined if m^{6}A-mRNA is required for DF2 localization to P-bodies. P-bodies are readily detected in wild-type and *Mettl14* knockout mES cells using the EDC4 P-body marker (Fig. 3d). However, in *Mettl14* knockout cells, DF2 was diffusely cytosolic with no clear P-body enrichment (Fig. 3d). Thus, DF2 is guided to P-bodies by forming complexes with m^{6}A-mRNA.

To further determine if polymethylated m^{6}A RNAs promote LLPS in cells, we measured m^{6}A levels in purified heat shock and arsenite stress granule mRNA (Fig. 4a, Extended Data

Fig. 4a,b). In both cases, m^{6}A levels in stress granule mRNA was ~45%−50% higher than in total cellular mRNA.

We also examined the transcriptomes of various RNA granules. We first examined biotin-isoxazole-induced RNA granules from mouse brain extracts, which resemble neuronal RNA granules[23]. In the previous transcriptomic analysis of these structures, the $\log_2$-fold enrichment for each mRNA was reported when it was greater than 1. We classified each mRNA based on the number of mapped m^{6}A sites. mRNAs with 0 mapped m^{6}A sites showed the lowest enrichment, while mRNAs with more mapped m^{6}A sites showed correspondingly higher enrichment (Extended Data Fig. 4c). Thus, polymethylated RNAs exhibit the highest enrichment in these RNA granules.

We observed a similar effect for arsenite-induced stress granules prepared from U2OS cells[24]. mRNAs with 0 or 1 mapped m^{6}A sites show no substantial enrichment in stress granules (Fig. 4b). However, for mRNAs with two or more m^{6}A sites, the degree of enrichment in stress granules increases in proportion to the number of mapped m^{6}A sites (Fig. 4b). A similar trend was seen using a transcriptomic analysis of stress granules induced with heat shock, thapsigargin, and arsenite in mouse embryonic fibroblast NIH3T3 cells[25] (Extended Data Fig. 4d). Although transcript length is correlated with increased enrichment in stress granules[24,25], the number of m^{6}A sites correlates with stress granule enrichment even when transcript length is controlled for (Extended Data Fig. 4e). Single-molecule fluorescence *in situ* hybridization showed that m^{6}A-containing mRNAs exhibit higher levels of stress granule enrichment than non-methylated mRNAs (Fig. 4c,d). Overall, these data show that polymethylated mRNAs, but not singly methylated RNAs, are enriched stress granules. Importantly, mRNAs lacking m^{6}A can be enriched in stress granules (Fig. 4b), suggesting they can also be recruited through m^{6}A-independent mechanisms.

It is possible that phase partitioning of DF-m^{6}A-mRNA complexes to different phase-separated compartments would impart a different fate to m^{6}A-mRNAs. In the case of unstressed cells, the targeting of DF proteins and m^{6}A-mRNA to P-body proteins facilitates m^{6}A-mRNA degradation[26]. We therefore asked if the relocalization of DF proteins and m^{6}A-mRNA to stress granules affects mRNA abundance. Examination of cellular mRNA levels using RNA-Seq in wild-type mES cells before, immediately after heat shock, or after a 1 h recovery period, showed no substantial alteration in the expression of m^{6}A-modifed mRNAs (Fig. 4e, Extended Data Fig. 5a, Supplementary Table 1). These data suggest that DF-m^{6}A-mRNA complexes in stress granules do not induce mRNA degradation.

We used ribosome profiling to compare translation efficiency of mRNAs when they contain m^{6}A, i.e., in wild-type cells, relative to when they lack m^{6}A, i.e., *Mettl14* knockout cells. In this way, we can determine the effect of m^{6}A on each mRNA in the dataset. Prior to heat shock, we found no substantial effect of m^{6}A on translation efficiency (Fig. 4f, Supplementary Table 2). As expected, ribosome-protected fragments were markedly reduced after 30 min of heat shock, consistent with global translational suppression reported during most stresses[27] (Extended Data Fig. 5b). However, translation was detectable 1 hr after cessation of heat shock (Extended Data Fig. 5c,d). At this time point, transcripts containing four or more m^{6}A sites showed significantly reduced translational efficiency in wild-type

relative to knockout cells (Fig. 4g, Supplementary Table 2). Thus, polymethylated mRNAs are preferentially repressed, potentially as a result of their phase separation.

Our studies demonstrate that m^{6}A regulates the fate of cytosolic mRNA by scaffolding DF proteins, leading to the formation of phase-separated DF-m^{6}A-mRNA complexes that then partition into phase-separated structures in cells. This effect is especially efficient for polymethylated mRNAs which can scaffold multiple DF proteins. Thus, although mRNAs are targeted to diverse intracellular condensates through diverse RNA-RNA and RNA-protein interactions[28], the presence of m^{6}A further enhances the partitioning into these structures. Furthermore, singly methylated and polymethylated mRNAs have different fates which likely reflect their different abilities to promote LLPS. Notably, monomethylated and polymethylated mRNAs are linked to distinct cellular functions and biological processes, which may therefore enable LLPS to influence specific cellular processes by selectively affecting translation of mRNAs based on their polymethylation status (Extended Data Fig. 6a,b).

Unlike other forms of RNA-scaffolded LLPS, m^{6}A provides a mechanism for regulated phase separation based on the multivalency of m^{6}A. Since m^{6}A levels might vary in different disease, differentiation or signaling contexts[14,29], the phase-separated transcriptome will be encoded, in part, by the cell context-specific distribution and number of m^{6}A sites in each mRNA (Extended Data Fig. 7a,b). The efficiency of m^{6}A-dependent regulation of an mRNA will likely be determined by pathways that control the efficiency of DF protein LLPS.

METHODS

Cell culture

HEK 293T/17 (ATCC CRL-11268) cells, U2OS (ATCC HTB-96) cells, and NIH3T3 (ATCC CRL-1658) cells were maintained in DMEM (11995–065, ThermoFisher Scientific) with 10% FBS, 100 units ml^{-1} penicillin and 100 μg 00^{-1} of streptomycin under standard tissue culture conditions (37°C, 5.0% CO_2). Mycoplasma contamination in cells was routinely tested by Hoechst staining. *Mettl14* knockout and wild type mouse ES cells were previously described by Geula *et al.*[19] and were a generous gift of J. Hanna and S. Geula (Weizmann Institute of Science). ES cells were grown in Knockout DMEM (10829018, Invitrogen) with 15% heat inactivated FBS, 100 U ml^{-1} penicillin and 100 μg ml^{-1} of streptomycin, 200 mM L-glutamine, 1% non-essential Amino-Acid (Gibco 11140076), 50 μM β-mercaptoethanol (21985023, Gibco), 1000 U ml^{-1} mouse LIF (ESG1107, EMD Millipore), 3 μM GSK3 inhibitor CHIR99021 (04-0004-02, Stemgent), 1 μM MEK1 inhibitor PD0325901 (04-0006-02, Stemgent). Media was changed daily. Cells were cultured on 0.1% gelatin-coated (07903, StemCell Technologies Inc.) plates and grown under standard tissue culture conditions (37°C, 5.0% CO_2). Cells were passaged as needed using TrypLE Express (Life Technologies) according to the manufacturer's instructions.

Stress conditions were induced as follows: heat shock at 42°C for 30 min a water bath; arsenite stress with 0.5 mM of sodium arsenite (35000–1L-R, Fluka) for 30–60 min, as indicated; and thapsigargin stress with 10 μM for 3 h (mESCs) or 5 μM for 1.5 h (NIH3T3).

The outcome of all stress experiments was performed in duplicate or triplicate. Investigators were not sample-blinded, and no randomization of samples was performed.

Immunostaining

Cells were plated to reach 40–60% of confluency the following day on a 35 mm petri dish coated with poly-D-lysine (PG35GC-1.5–14-C). For mES cell culture and immunostaining, petri dishes were coated with gelatin for 1 h at 37°C. Cells were washed three times with PBS and fixed for 15 min with 4% paraformaldehyde in PBS. Cells were permeabilized and blocked with 0.2% triton X-100 and 2% FBS in PBS for 30 min at 25°C. Cells were incubated for 90 min with the primary antibody followed by washing three times in PBS. After washing, cells were incubated with secondary antibodies conjugated to Alexa Fluor 488 and/or Alexa Fluor 594 at 2 μg/mL in PBS (Life Technologies) for 60 min. Nuclei were stained with Hoechst 33342 (66249, Life Technologies) at a 0.1 μg/mL in PBS for 10 min. Coverslips were mounted using Prolong Diamond Antifade Mountant (P36961, Life Technologies). All immunostaining steps were carried out at 25°C.

DF2 localization in P-bodies was determined using the P-body marker EDC4. The large number of P-bodies seen in the *Mettl14* knockout cells compared to wild-type cells is due to the different morphology of *Mettl14* knockout cells. As described previously for *Mettl3* knockout and other m^6A-deficient cells, m^6A-depleted cells are flattened, while wild-type cells are “dome-shaped”[33,34]. As a result, in a single confocal slice, more P-bodies are seen in *Mettl14* knockout cells. In contrast, since wild-type cells are dome shaped, there are many more z-stacks, and the P-bodies are found throughout the different confocal slices. However, overall, there is no substantial difference in the number of P-bodies in wild-type and *Mettl14* knockout cells.

The puromycin time course experiment was performed as follows: cells were heat shocked at 42°C in a water bath for 30 min and incubated with 10 μg/mL of puromycin before each time point for 10 min and then washed with PBS and fixed with 4% paraformaldehyde. Staining was performed using anti-TIAR (5137S Cell Signaling Technology) and anti-puromycin (NC0327811, Millipore Sigma) antibodies.

Protein expression and purification

N-terminal 6X-His tagged DF1, DF2, DF3 and YTH domain were generated by standard PCR-based cloning strategy from HEK293T oligo-d(T)25-primed cDNA as described previously[35]. DF proteins and the YTH domain were overexpressed in *E. coli* Rosetta2 (DE3) single (Novagen) using pET-28(+) (Novagen) or pProEx HTb (Invitrogen). *E. coli* expressing DF proteins and the YTH domain were induced with 0.5 mM isopropyl β-D-1-thiogalactopyranoside (IPTG) for 16 h at 18°C. Cells were collected, pelleted and then resuspended in the following buffer: 50 mM NaH_2PO_4 pH 7.2, 300 mM NaCl, 20 mM imidazole at pH 7.2 and supplemented with EDTA-free protease inhibitor cocktail (05892791001, Roche) according to the manufacturer’s instructions. The cells were lysed by sonication and then centrifuged at 10,000 × *g* for 20 min. The soluble protein was purified using Talon Metal Affinity Resin (Clontech) and eluted in the following buffer: 50 mM NaH_2PO_4 pH 7.2, 300 mM NaCl, 250 mM imidazole-HCl at pH 7.2. Further concentration

and buffer exchange was performed using Amicon Ultra-4 spin columns (Merck-Millipore). Recombinant protein was stored in the following buffer: 20 mM HEPES pH7.4, 300 mM KCl, 6 mM $MgCl_2$, 0.02% NP40, 50% glycerol at −80°C or 20% glycerol at −20°C. All protein purification steps were performed at 4 °C. The purified protein was quantified using a ND-2000C NanoDrop spectrophotometer (NanoDrop Technologies) with OD 280 and verified by Coomassie staining.

Protein labeling

For DF phase separation experiments, DF1, DF2 and DF3 proteins were fluorescently labeled using Alexa Fluor (488, 594 and 647, respectively) Microscale Protein Labeling kit according to the manufacturer's instruction (A30006, A30008, A3009, Thermo Fischer Scientific). Briefly, DF proteins were diluted at 1 mg/mL in PBS and mixed with 100 mM sodium bicarbonate. The reaction was incubated for 15 min at room temperature and fluorescently labeled proteins were purified from the unreacted dye substrate by column purification using Micro Bio-Spin Columns with P-30 gel. The labeled protein was eluted in 20 mM HEPES pH 7.4, 300 mM KCl, 6 mM $MgCl_2$, 0.02% NP-40 and buffer exchange was performed in two successive rounds using Amicon 0.5 mL Ultracel centrifugal filter columns. Protein labeling was performed the day of each experiment.

Droplet formation

DF2 was purified as described previously[36]. Temperature-dependent droplet assembly was performed in the following buffer: 20 mM HEPES pH 7.4, 300 mM KCl, 6 mM $MgCl_2$, 0.02% NP-40. For non-fluorescent DF2 (75 μM), droplet-containing buffer was placed on a coverslip and visualized by either phase contrast or differential interference contrast (DIC) microscopy using a Nikon TE-2000 inverted microscope. Temperature-dependent phase separation experiments were performed by incubating DF2 at 37°C for 1 min after removal from ice. The temperature-dependent phase-transition diagram was generated by visualizing droplets using phase-contrast microscopy on a coverslip incubated in a temperature, humidity, and CO_2 controlled top stage incubator (Tokai Hit). Temperature was increased from 22 to 37°C at a rate of 1°C per minute and images were taken every 30 seconds.

RNA-dependent droplet formation experiments were performed in the following buffer: 10 mM HEPES pH 7.4, 150 mM KCl, 3 mM $MgCl_2$, 0.01% NP-40, and 10% glycerol. 25 μM of DF2 diluted in buffer was placed on a cover slip and RNA containing 0, 1, or 10 m^6A was added (570 nM). The solution was incubated at 37°C for 10 min and droplets were visualized with phase-contrast microscopy.

The salt-dependent phase separation was generated by combining diluted DF2 protein (1–8 μM) with NaCl buffer (20 mM HEPES pH 7.4, 300 mM KCl, 6 mM $MgCl_2$, 0.02% NP-40, 50% glycerol, with NaCl) on a coverslip and scoring yes/no for the presence of protein droplets as previously described[37] by observation using a bright field microscope.

In vitro transcription

To synthesize RNAs containing a single m^6A or A nucleotide, or 10 m^6A or 10 A nucleotides, we performed in vitro transcription using reactions that contained either m^6A

triphosphate or adenosine triphosphate. This approach ensures that all adenosines are either in the m^{6}A or A form. In vitro transcription was performed using AmpliScribe T7 High Yield Transcription kit (AS3107, Lucigen) according to the manufacturer's instruction. The template encodes an RNA containing a single adenosine (indicated in bold): (GGTCTCGGTCTTGGTCTCTGGTCTTTGG**A**CTTGGTCTTGGTCTTCGGTCTCGGTC TTTGGTCT) or 10 adenosines in the canonical GGACU consensus motif for m^{6}A: (GG**A**CTCGG**A**CTTGG**A**CTCTGG**A**CTTTGG**A**CTTGG**A**CTTGG**A**CTTCGG**A**CTCGG**A** CTTTGG**A**CT). The m^{6}A versions of the RNA were synthesized by replacing adenosine 5' triphosphate in the reaction by N6-methyadenosine 5' triphosphate (TriLink). The reaction was terminated by addition of DNAse I and incubation for 15 min at 37°C. RNA was purified using an Oligo Clean and Concentrator column (D4061, Zymo Research). RNA concentration was determined using a NanoDrop spectrophotometer and verified by TBE-urea denaturing gel electrophoresis. Nucleic acid staining was performed with SYBR Gold (S11494). DNA matrix was obtained by hybridizing DNA oligonucleotides containing a T7 promoter and the target sequence.

For fluorescent RNA in vitro transcription, BODIPY FL-Guanosine 5'-O-(3-Thiotriphosphate) fluorescent GTPs (G22183, Invitrogen) were added to the reaction in a 1:10 molar ratio with GTPs. The thiotriphosphate linkage prohibits the fluorescent nucleotides from being internally incorporated, and only allows incorporation at the +1 position of *in vitro* transcripts (the initial 'G' after the T7 promoter sequence). Incorporation of the fluorescent GTP into transcripts was verified by TBE-urea denaturing gel electrophoresis and fluorophore excitation by exposure to 488 nm light. RNA concentrations were determined using a NanoDrop spectrophotometer and verified by SYBR Gold staining.

Partition coefficients

For partition coefficient experiments with Alexa488-labeled DF proteins, DF proteins (15 μM) were mixed in a buffer containing 20 mM HEPES 7.6, 300 mM KCl, 6 mM $MgCl_2$, 0.02% NP-40., and 50% glycerol. Upon addition of 425 nM RNA containing 10 m^{6}A nucleotides, the reaction was held at 37°C for approximately 10 minutes. DF-containing droplets were then imaged at 40x using a bright field microscope. Partition coefficients for the no RNA condition were calculated by creating a ratio of DF intensity in solution over DF intensity located in the immediately adjacent region. After DF2 droplet enrichment following the addition of m^{6}A-RNA, partition coefficients were calculated for stably-formed DF-containing droplets. Follow-up partition coefficient calculations were performed approximately 24 hours after initial DF2-enriched droplet formation.

For fluorescent m^{6}A-RNA partition coefficients, fluorescent RNAs (850 nM) were mixed with a solution containing 7.5 μM DF2 in buffer containing 10 mM HEPES 7.6, 150 mM KCl, 3 mM $MgCl_2$, 0.01% NP-40., and 10% glycerol. Formation of fluorescent DF2:m^{6}A-RNA coacervates was visualized by fluorescence microscopy within minutes. Partition coefficients were calculated by taking the ratio of fluorescence intensity of soluble fluorescent m^{6}A-RNA over m^{6}A-RNA-enriched DF2 droplets and adjacent regions.

For *in vivo* DF2 intensity ratios in mES cells, TIAR staining was used to demarcate stress granule boundaries. ROIs were manually drawn to encompass a central portion of the TIAR-

positive stress granules and the fluorescence intensity values for DF2 in these regions were averaged. Intensity ratios of DF2 staining immediately adjacent to the TIAR-positive stress granules in an identical ROI were used as background. Intensity ratios were then determined by calculating the average phase separated DF2 intensity inside stress granules over the average soluble DF2 intensity in the immediately adjacent cytoplasm.

Determination of relative m^{6}A levels by two-dimensional thin layer chromatography

Experiments measuring m^{6}A in stress granules and in the cytosol were performed and analyzed by an investigator blinded to the sample identity. Relative levels of internal m^{6}A in mRNA were determined by thin-layer chromatography (TLC) as described previously[38]. This method selectively examines m^{6}A in the mRNA sequence context, thereby preventing problems with contamination of the m^{6}A signal by copurifying rRNA or snRNA. Additionally, levels of adenosine in the poly(A) tail are not measured since only nucleotides (methylated or nonmethylated) that are followed by G are detected in this assay. Briefly, twice purified poly(A) RNA was digested with 2 U of RNase T1 (ThermoFisher Scientific) for 2 h at 37°C in the presence of RNAseOUT (Invitrogen). Digested 5′ ends RNA were subsequently labeled with 10 units of T4 PNK (NEB) and 0.4 mBq [γ–^{32}P] ATP for 30 min at 37°C followed by removal of the γ-phosphate of ATP by incubation with 10 U apyrase (NEB) at 30°C for 30 min. After phenol-chloroform extraction and ethanol precipitation, RNA samples were resuspended in 10 µl of DEPC-H_2O and digested to single nucleotides with 2 units of P1 nuclease (Sigma) for 3 h at 37°C. 1 µl of the released 5′ monophosphates from this digest were then analyzed by 2D TLC on glass-backed PEI-cellulose plates (MerckMillipore) as described previously[38]. No m^{6}A was detected in *Mettl14* knockout poly(A) RNA consistent with mass spectrometry data obtained from this cell line previously[19].

Synthesis and cloning of mNeonGreen ORF

mNeonGreen protein-coding open reading frame (ORF) was *in vitro* synthesized using overlapping 60-mer DNA oligonucleotides designed using DNAWorks[39]. Briefly, a *Hind* III restriction site-deficient, human codon-optimized DNA sequence for mNeonGreen protein sequence (GenBank: AGG56535.1) and 60-mer overlapping DNA oligos were generated using DNAWorks. The ORF was synthesized in two PCR reaction steps. In the first PCR, oligo assembly PCR amplification was performed by mixing the overlapping oligos at 2 µM in 1X Phusion HF master mix (NEB, cat. # M0531S) and PCR cycling at 98°C for 30 s; 25 cycles of 98°C for 5 s, 64°C for 20 s, 72°C for 20 s; 72°C for 10 s; 4°C hold. One microliter of oligo assembly PCR was subjected to a second PCR where the open reading frame was amplified using mNeonGreen forward (ATA TAA GCT TGA TAT GGT GAG TAA GGG CGA AGA GGA) and reverse (ATA TAA GCT TTT TAT ACA ACT CGT CCA TGC CCA TCA CG) primers in 50 µl of 1X Phusion HF master mix and the following thermal cycling conditions: 98°C for 30 s; 30 cycles of 98°C for 5 s, 64°C for 20 s, 72°C for 20 s; 72°C for 10 s; 4°C hold. The amplified PCR product (of 731 bp) was gel eluted, digested with *Hind* III, and cloned at *Hind* III site at pcDNA™4/TO Mammalian Expression Vector (ThermoFisher Scientific, cat. # V102020). Bacterial clones containing mNeonGreen ORF in the correct orientation were selected by DNA sequencing. This plasmid is referred to as pcDNA-4TO-mNeonGreen.

Cloning and generation of DF2 and DF2 mutant plasmids

Human DF2 was PCR amplified using DF2-BamHI-F (ATA TGG ATC CAT GTC GGC CAG CAG CCT CTT) and DF2-XhoI-R (GGT GCT CGA GCT ATT TCC CAC GAC CTT GAC GTT CCT T) oligonucleotides using human cDNA made by oligo dT-priming HEK-293T total RNA. PCR product was gel eluted and digested and cloned at *Bam* HI and *Xho* I in pcDNA-4TO-mNeonGreen plasmid. W432A mutation was introduced using DF2-W432A-SDM-F (GCG TGC AGC ACA GAG CAT GG) and DF2-W432A-SDM-R (AAT ATT ATA CTT AAT GGA ACG GTG AAT ATC GTC C) oligonucleotides in 1X Phusion HF master mix.

CRISPR/Cas9 knock-in of NeonGreen into the endogenous *YTHDF2* locus

For FRAP experiments of DF2 in stress granules, NeonGreen was CRISPRed into the endogenous locus since plasmid-based expression of DF2 in HEK293 cells is associated with ectopic granule formation. Knock-in by CRISPR was performed as described previously[40]. The sequence of the guide RNA used is (TGTAGGAACGTCAAGGTCGT). For these experiments we generated a single-stranded homology directed repair DNA template containing 800 nucleotide-long homology arms flanking a NeonGreen coding sequence immediately prior to the stop codon of DF2. Successful incorporation was validated by western blotting using a DF2-specific antibody for DF2-NeonGreen which exhibited the expected mobility shift relative to DF2.

Antibodies

The following antibodies were used for immunofluorescence experiments: rabbit anti-TIAR (5137S, Cell Signaling Technology, Lot #1, 1:100), mouse anti-TIAR (Clone 6) (610352, BD Biosciences, Lots #5357680; 7219778, 1:100), mouse anti-Edc4 (H-12) (sc-376382, Santa Cruz Biotechnology, Lot #I0216, 1:100), mouse anti-Puromycin clone 12D10 (MABE343, Millipore Sigma, Lot #2861354, 1:100), rabbit anti-G3BP1 (13057–2-AP, Proteintech, Lot #00047654, 1:100), mouse anti-ATXN2 (Clone 22) (611378, BD Biosciences, Lot #7341666, 1:100), rabbit anti-YTHDF1 (17479-AP, Proteintech, Lot #00040713, 1:100), rabbit anti-YTHDF2 (24744–1-AP, Proteintech, Lot #00053880, 1:100), rabbit anti-YTHDF3 (ab103328, Abcam, Lot #GR35115–39, 1:100), rabbit anti-IgG Alexa Fluor 594 (A11012, Invitrogen, Lot #1933366, 1:1000), mouse anti-IgG Alexa Fluor 488 (A11001, Invitrogen, Lot #1939600, 1:1000).

The following antibodies were used for immunoblotting experiments: rabbit anti-YTHDF2 (ARP67917_P050, Aviva System Biology, Lot #QC38405–43182, 1:1000), mouse anti-GAPDH (SC-365062, Santa Cruz Biotechnology, Lot #A2816, 1:5000), rabbit anti-IgG HRP (NA934V, GE Healthcare, Lot #16677077, 1:10000), mouse anti-IgG HRP (NA931V, GE Healthcare, Lot #16814909, 1:10000).

Overexpression of DF2 in mES cells

Mettl14 wild type and knockout mES cells were transfected with NeonGreen-tagged DF2 and DF2 W432A-expressing plasmids using Fugene HD transfection Reagent (E2311, Promega) according to the manufacturer's instructions. Briefly, cells were plated on 35 mm glass-bottom dishes coated with poly-D-lysine (PG35GC-1.5–14-C) and 1% gelatin and

allowed to reach 40 to 60% confluency the following day. 48 h after transfection, plates were placed in a temperature, humidity, and CO_2-controlled stage-top incubator for live cell imaging (Tokai Hit) and cells were imaged by fluorescence microscopy. Importantly, expression of DF2 in mES cells was not associated with ectopic formation of granules as can be seen in the images. This contrasts with HEK293 cells and other cell types, where we found that DF2 expression caused the formation of granules. We therefore performed these experiments in mES cells. mES cells were then heat shocked at 42°C in a water bath for 30 min. Cells were then washed twice with PBS, fixed for 15 min with 4% paraformaldehyde, and again washed twice with PBS before visualizing by fluorescence microscopy.

Single molecule FISH

Cells were plated to reach 40–60% confluency the following day on a 35 mm petri dish coated with poly-D-lysine. For mES cell culture and immunostaining, petri dishes were coated with gelatin for 1 h at 37°C. Single molecule fluorescence of mRNA was performed using the ViewRNA Cell Plus Assay kit (Invitrogen, 88–19000). All steps were carried out according to manufacturer's instructions. An Alexa 594- and Alexa 647-labeled ViewRNA probes (Invitrogen) was used to detect the presence of nonmethylated and polymethylated mRNAs in the same cell sample. TIAR was stained as a stress granule marker. Wild type mES cells (n=15) were analyzed by confocal microscopy.

For smFISH, we compared the non-methylated mRNAs *Grk6* (length = 2994 nt, normalized RNA-seq counts = 712), and *Polr2a* (length = 6740 nt, normalized RNA-seq counts = 2963), and compared them with matched m^6A-containing mRNAs *Fignl1* (length = 2974 nt, normalized RNA-seq counts = 892; 4 annotated m^6A peaks[19]) and *Fem1b* (length = 6785 nt, normalized RNA-seq counts = 2396; 4 annotated m^6A peaks[19]). Probes were labeled with different fluorophores so that comparisons of stress granule localization could be performed in the same cells for each matched probe pair.

Western Blotting

Cells were lysed in whole cell lysis buffer (10 mM Tris-HCl pH 7.4, 10 mM EDTA, 50 mM NaF, 50 mM NaCl, 1% Triton X-100, 0.1% SDS, with 1X protease and phosphatase inhibitor (78440, Pierce)) and sonicated. Protein quantification was performed using the Pierce BCA protein assay kit according to the manufacturer's instruction (23227, Thermo Fisher Scientific). Equal quantities of proteins were separated on 4–12% Bis–Tris gels (Invitrogen) and transferred onto a nitrocellulose membrane for 1 h at constant 30 V at 4°C. Membranes were blocked by incubation in 5% milk in TBS-T for 1 h at room temperature under agitation. Membranes were stained with primary antibodies, extensively washed in TBS-T and then incubated with appropriate secondary antibodies conjugated to HRP. Blots were imaged on a ChemiDoc XRS+ system (Bio-Rad).

RNA-seq analysis

mES cells were plated on a 10 cm dish and allowed to reach 70–80% confluence. Heat shock was performed for 30 min in a water bath at 42°C. In order to measure RNA expression after stress, heat-shocked cells were placed back at 37°C for 1 h. After collecting cells as described in the Ribo-seq section, 5% of the lysate cells before RNase digestion was

used to extract Total RNA. Library preparation was performed using the NEBNext Ultra Directional RNA Library Prep Kit starting from 1 μg of total input RNA and following the protocol for use with NEBNext rRNA Depletion Kit. The libraries were sequenced on the Illumina HiSeq 2500 instrument, in single-read mode, with 50 bases per read. A separate independent biological replicate was sequenced for each Ribo-seq replicate to have a mate for TE analysis for each Ribo-seq library.

After sequencing, fastq files were trimmed for quality and read lengths shorter than 16 nt were discarded. The adapter was removed using FLEXBAR[41]. Duplicates were removed with the pyFastDuplicateRemover.py utility from the PyCRAC software suite as previously described[41]. Ribosomal reads were removed using STAR aligner[42]. The remaining reads were mapped to the mm10 genome using STAR and the data were used to normalize the Riboseq data for the translational efficiency measurements. A pseudocount of 0.001 was added to avoid division by zeroes. Differential expression analysis of RNA-seq data was performed with the DESeq2 package in R. Differential expression data used to generate the plots for Fig. 4e and Ext. Data 5a are available in Supplementary Table 1. Raw data are available at NCBI GEO: GSE125725.

Ribosome profiling

Ribosome profiling was performed essentially as previously described[43]. Briefly, mES cells were plated on a 10-cm dish and allowed to reach 70–80% confluence. Heat shock was performed for 30 min in a water bath at 42°C. To measure translation after stress, heat shocked cells were placed back at 37°C for 1 h to enable translation to resume. To inhibit ribosome transit post-lysis, cells were rapidly washed twice with ice-cold PBS containing 50 μg/ml of cycloheximide. To generate ribosome-protected fragments, cells were pelleted and immediately lysed in 400 μL of cell lysis buffer (20 mM Tris pH 7.4, 150 mM NaCl, 5 mM $MgCl_2$, 1 mM DTT, 100 μg/mL cycloheximide, 25 U DNase I). Lysate was clarified by performing a centrifugation step at 20,000 g for 10 minutes at 4°C. Supernatant was collected. A 5% fraction of this supernatant was used for RNAseq preparation. 30 μg of RNA were used to isolate ribosome-protected fragments following RNase I digestion. After RNase digestion, lysates were loaded on a sucrose gradient and centrifuged at 100,000 rpm to recover ribosome-protected fragments. RNA from the resuspended ribosomal pellet was purified and run on a gel to selectively excise foot-printed RNAs (from 17 nt to 34 nt RNA fragments).

To avoid any ribosomal contamination in the library preparation steps, we then performed Ribo-Zero Gold depletion of the foot-printed RNA. The rRNA depleted RNA fragments were dephosphorylated and the linker was added. To specifically deplete unligated linker, yeast 5'-deadenylase and RecJ exonuclease digestion was performed. At this point, the library preparation steps were performed essentially as previously[41]. Briefly, reverse transcription was performed using SuperScript III. To avoid untemplated nucleotide addition, reverse transcription was carried out at 57°C, as previously described[43]. cDNA purification, circularization, and amplification were performed as previously described[41]. Libraries were sequenced with a single-end 50 bp run using an Illumina Hiseq2500 platform. Generation of the sequencing libraries was from four separately purified biological

replicates. After sequencing, fastq files were quality-based trimmed and reads below 16 nt were excluded. The adaptor was removed using the FLEXBAR tool[41]. The demultiplexing was performed on the basis of the experimental barcode using the pyBarcodeFilter.py script[41]. The second part of the iCLIP random barcode was then moved to the read header (awk -F "##" '{sub(/…./,"##"$2, $2); getline($3); $4 = substr($3,1,2); $5 = substr($3,3); print $1 $2 $4"\n"$5}').

After removal of the PCR duplicates, ribosomal and mitochondrial RNA reads were removed using STAR aligner[42]. Reads with no acceptable alignment to ribosomal and mitochondrial RNA were then mapped to the mm10 transcriptome. We specifically considered only ribosome protected fragments reads mapped to the coding sequence to avoid any possible contamination coming from the untranslated area of the genome. Given our interest in studying translation independently from the initiation/stopping rates, we excluded ribosomes protected fragments mapping to the first 15 amino acids and the last 5 amino acids of each coding sequence. Only the longest splice isoform of each gene was considered. Gene count tables for ribosome protected fragments and RNA-sequencing reads from each sample were then normalized and processed using the xtail package in R to calculate translational efficiency[44]. To remove the background, genes with fewer than 4 minimum mean ribosome protected fragment read were excluded. Replicates that included <50% mapped coding sequence reads were excluded from the final analysis. *Mettl14* knockout cells were used as the normalizing condition. Translational efficiency tables used to generate the plots in Fig. 4f–g are available in Supplementary Table 2. Raw data can be accessed at NCBI GEO: GSE125725. Each gene with an assigned $\log_2$-fold change was annotated for the presence of an m^{6}A site using a previous m^{6}A mapping study[19].

Analysis of enrichment of methylated RNAs in stress granules.

For U2OS cells, stress granule gene expression data (GSE99304) and m^{6}A MeRIP-seq data (GSE92867) were downloaded from the NCBI Gene Expression Omnibus (GEO). For NIH3T3 cells, stress granule gene expression data (GSE90869) and m^{6}A MeRIP-seq data (GSE61998) were downloaded from GEO. The m^{6}A bed file was processed to produce a table of m^{6}A peak counts per gene. The gene expression data was extracted from the FPKM columns for the stress granule and total cell fractions. A pseudocount of 0.001 was added to the expression values to avoid division with 0. The enrichment score was calculated as $\log_2$ (stress granule FPKM/total cell FPKM). The cumulative distribution function was calculated for genes grouped by m^{6}A count and plotted using R.

The abundance of DF proteins stated in the average cell is calculated from an analysis of absolute protein abundance in different cell lines using a proteomic approach[8]. Based on a reported number of ~740,000 copies of DFs per PC3 cancer cell and an average cytosolic volume of ~2,300 μM, we estimate DFs to be at approximately ~5.3 μM in the cell.

FRAP analysis

For *in vitro* FRAP analysis, fluorescent DF2 droplets loaded into a cell counter slide (C-Chip DHSC-N01 iN Cyto) at room temperature. The droplet was photobleached in 3 regions of interest (ROI) that were defined for these experiments. ROI-1 was the indicated circular

region in the droplet, and ROI-2 was a similarly sized circular region in the same droplet but in an area which was not photobleached. ROI-3 was defined as background and drawn outside the droplet and its signal was subtracted from both ROI-1. Raw data were plotted using Prism Software.

For FRAP experiments of the stress granules in living cells, the entire stress granule was chosen as the ROI in order to more accurately quantify the ability of DF2-NeonGreen to phase separate from the cytoplasm into the stress granule. Unlike the in vitro experiments above which involved DF2 droplets that could reach sizes of 10–20 μM in diameter, stress granules in vivo are < 1 μM and mobile. Thus, rather than photobleaching the center, the entire stress granule was photobleached. Data were normalized to the frame with the highest average ROI intensity level. Bleached granules were subjected to 514 nm laser burst for 1.03 μs at frame 0. Each frame taken after bleaching represents 3.5 s of recovery. Each data point is representative of the mean and standard deviation of fluorescence intensities in three unbleached (control) or three bleached (experimental) granules.

Gene ontology of U2OS cells

Gene ontology analysis was performed using the PANTHER Gene Enrichment Analysis tool at www.geneontology.org[45]. U2OS RNA-seq counts from GSE99304[24] and m^{6}A MeRIP-seq data from GSE92867[32] were used to generate the input data. Genes that lacked any annotated m^{6}A sites were classified as having zero sites. For the singly methylated GO, genes with one mapped m^{6}A site were compared to genes with zero mapped m^{6}A sites. For the polymethylated GO, genes with four or more mapped m^{6}A sites were compared to genes with zero mapped m^{6}A sites. P-values were calculated using Fisher's Exact Test with a Bonferroni correction for multiple hypothesis testing. The top twelve genes by p-value are charted for each gene ontology category. The minimum p-value for inclusion was $p < 0.01$.

Protein disorder propensity plots for YTHDF proteins

Protein disorder propensity plots for the YTHDF proteins were prepared using the PLAAC (Prion-like amino acid composition) webtool with background set to 0%[46]. Determination of the amino acid composition by percent was performed using the ProtParam tool from ExPASy (https://web.expasy.org/protparam/) and amino acid composition bar charts were made using ggplot2 in R.

Image acquisition and analysis

Fluorescence imaging and bright field imaging experiments were performed using a wide-field fluorescent microscope (Eclipse TE2000-E microscope, Nikon). Images were analyzed using NIS-Elements Viewer software (Nikon), and Fiji (ImageJ v1.51n) for quantification analysis.

FRAP experiments were performed using LSM 880 Microscope Laser Scanning Confocal Microscope (Zeiss) Airyscan High Resolution Detector connected to temperature, humidity, and CO_2 controlled top stage incubator for live cell imaging (Tokai Hit). Differential Interference Contrast images were taken with a Zeiss Axioplan 2 Upright Microscope.

smFISH and P-body experiments were performed using an LSM 880 Microscope Laser Scanning Confocal Microscope (Zeiss) Airyscan High Resolution Detector. Z-stacks were taken at 63x oil immersion objective. Images were analyzed using ZEN Black software (Zeiss) and Fiji (ImageJ v1.51n). Co-localization and 3D analysis of confocal Z-stacks for smFISH experiments was performed using the DiAna plugin for ImageJ[47]. Granules from 5 images with 3–5 cells per image were analyzed using this high-throughput method, which allowed us to simultaneously measure smFISH and TIAR antibody signal colocalization for as many as 100 smFISH puncta in a single confocal Z-stack. Using this method, the total number of data points from the images for each smFISH probe were scored as a ratio of puncta colocalizing with TIAR-containing stress granules over the fraction of total puncta detected in the cell.

Statistics and reproducibility

All statistical analyses were performed in GraphPad Prism 8 or Microsoft Excel unless otherwise indicated. The outcomes of all statistical tests including p-values and number of samples are included in the figure panels or corresponding figure legends. Significance was defined as any statistical outcome that resulted in a $p < 0.05$, unless otherwise indicated. P-value significance is represented by the following: *$p < 0.05$, **$p < 0.01$, ***$p < 0.001$, ****$p < 0.0001$. Multiple hypothesis correction and p-value adjustments were not performed unless otherwise indicated.

Temperature-dependent DF phase separation experiments (Fig 1a, b) were performed in duplicate on biological replicates. Salt-dependent DF2 phase separation experiments (Fig. 1c) were performed in duplicate on technical replicates. Droplet formation assays with Alexa488-labeled DF proteins (Fig 1d, Extended Data 1b–e) were performed in duplicate on biological replicates. Fluorescence recovery after photobleaching of Alexa488-DF2 was performed on 8 droplets in technical replicates. Validation of m^6A RNA (Extended Data 1f) was performed in duplicate from technical replicates. m^6A RNA dependent phase separation experiments (Fig. 1f–g, Extended Data g-h) were performed in duplicate on biological replicates. Staining of DF2 and stress granule markers in mES cells (Fig. 2a–b, Extended Data 2a) were performed in triplicate on three biological replicates. Staining of DF1 and DF3 with stress granule markers in mES cells (Extended Data b-c) was performed in duplicate on biological replicates. Staining of DF2 and TIAR in HEK293, U2OS, and NIH3T3 cells (Extended Data d-f) was performed in duplicate on biological replicates. Western blot of CRISPR/Cas9-edited YTHDF2-NeonGreen edited cells (Extended Data 2g) was performed in duplicate on technical replicates. Imaging of DF2-NeonGreen stress-induced granules (Extended Data 2h) was performed in duplicate on biological replicates. Fluorescence recovery after photobleaching in DF2-NeonGreen cells (Fig. 2c) was performed on three granules in one biological sample. DF2 and EDC4 co-staining in mES cells (Fig. 1d) was performed in duplicate in biological replicates. DF2 staining after puromycin or actinomycin D treatment (Extended Data 2j) was performed in duplicate on biological replicates. Thin-layer chromatography of stressed NIH3T3 cells (Extended Data 2k–l, Fig. 4a, Extended Data 4b) was performed in triplicate in three biological replicates for control conditions, and quadruplicate for four biological replicates in stress conditions. Staining of DF2 in stressed WT and Mettl14 KO mES cells (Fig. 3a–b, Extended Data 4b)

was performed in triplicate on three biological replicates. Thin-layer chromatography of poly(A)-purified mRNA from WT and Mettl14 KO mES cells (Extended Data 3a) was performed in duplicate on technical replicates. Transfection of NeonGreen-DF constructs (Fig. 3c) was performed in duplicate on biological replicates. Staining of EDC4 and DF2 in WT and Mettl14 KO mES cells (Fig. 3d) was performed in duplicate on biological replicates. Validation of stress granule isolation from NIH3T3 cells (Extended Data 4) was performed in duplicate on biological replicates. Cumulative distribution plots of m^6A-mRNAs from stress granules in U2OS cells (Fig. 4b) were based on average values of RNA $\log_2$ fold change generated from three biological replicates. Cumulative distribution plots of m^6A-mRNAs from isoxazole-induced neuronal RNA granules (Extended Data 4c) were based on average values of RNA $\log_2$ fold change generated from three biological replicates. Cumulative distribution plots of m^6A-mRNAs from stress granules in NIH3T3 cells (Extended Data 4d) were based on average values of RNA $\log_2$ fold change generated from three biological replicates. smFISH on mRNAs in mESC cells (Fig. 4c–d) were performed in duplicate in biological replicates. Analysis of RNA-seq from WT mES cells (Fig. 4e, Extended Data 5a) were performed on average $\log_2$ fold change values from four biological replicates. Total Ribo-seq coding sequence reads (Extended Data 5b) are from four biological replicates in each condition. Analysis of translational efficiency in WT mES cells vs. Mettl14 KO cells before stress (Fig. 4f) was performed on four and three biological replicates, respectively. Analysis of translational efficiency in WT mES cells vs. Mettl14 KO cells 1 hour after stress (Fig. 4g) was performed on four and two biological replicates, respectively. Translational recovery experiments (Extended Data 5c) were performed in duplicate on biological replicates. Pearson's correlation coefficients for Ribo-seq reads (Extended Data 5d) were performed on the top two biological replicates which was determined by samples with the highest percentage of mapped reads to the coding region.

Data availability

The accession number for the RNA sequencing (Fig. 4e, Extended Data 5a) and ribosome profiling (Fig. 4f, g; Extended Data 5b, d) data reported in this paper is NCBI GEO: GSE125725.

Extended Data

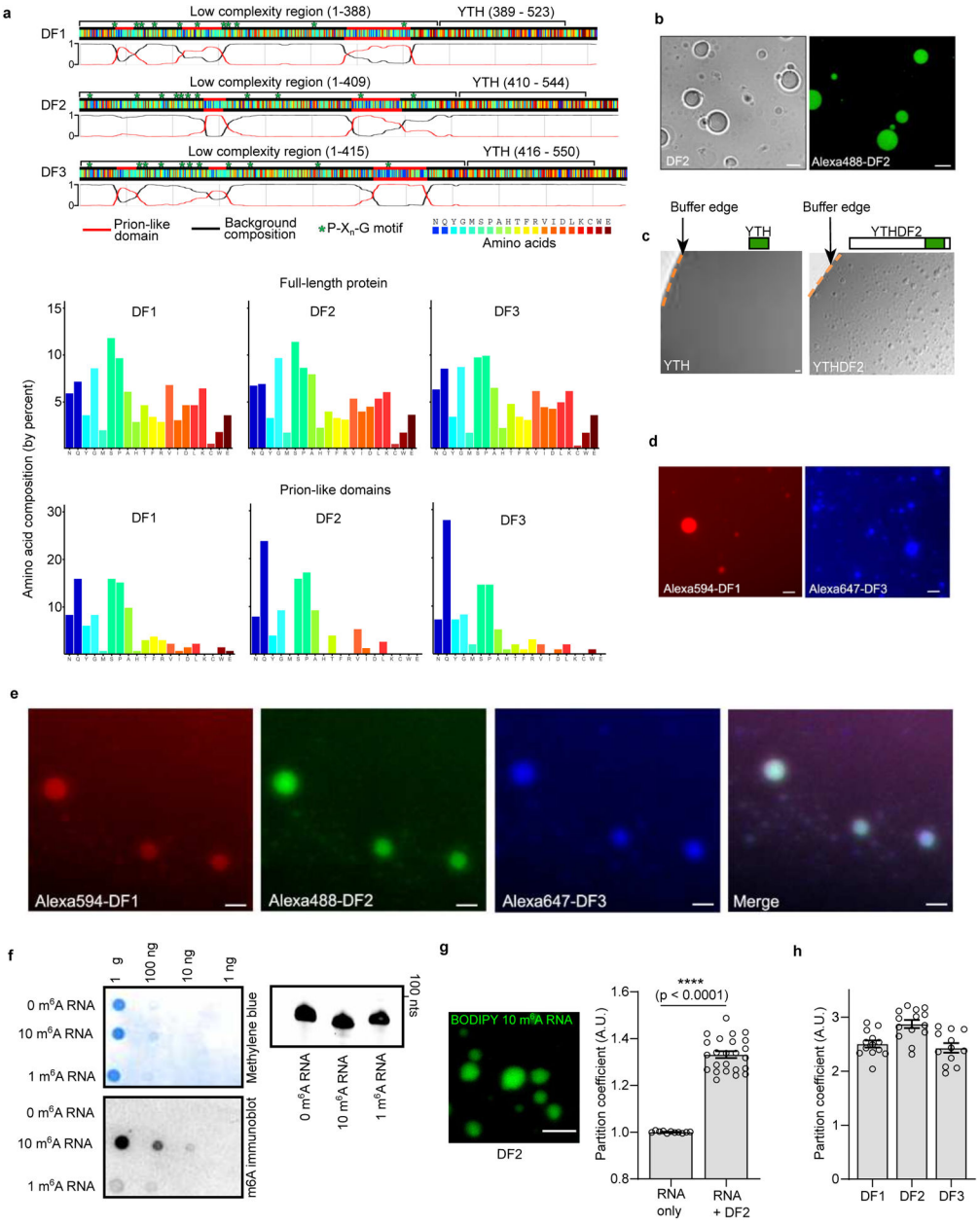

Extended Data Fig. 1. Fluorescent labeling of DF2 does not affect liquid droplet formation

a, DF1, DF2 and DF3 exhibit high sequence homology. Shown is a color-coded schematic representation of the aligned amino acid sequence and corresponding prion-like domain disorder propensity plots (red and black traces) for DF1, DF2 and DF3 generated using the PLAAC (Prion-like amino acid composition) tool[46]. The y-axis of the plot represents prion-like regions (1) and regions of background amino acid composition (0). The low complexity domain is a ~40 kDa region that contains glutamine-rich prion-like domains and an abundance of disorder-promoting residues such as proline, glycine, serine, alanine, and asparagine. These domains are also enriched with multiple P-X_n-G motifs that are known to be associated with lower critical solution temperature (LCST)[7]. The ~15 kDa YTH domain exhibits high sequence identity between the paralogs, and all YTH domains show identical

binding to m^{6}A without preference for any specific sequence context surrounding m^{6}A[4]. The high degree of sequence identity suggests that these proteins might function redundantly in stress granule formation and phase separation. Amino acid composition of the full-length DF proteins and their prion-like domains are shown in the bar charts at the bottom of the panel.

b, Liquid droplet formation of Alexa488-labeled DF2. The goal of this experiment is to confirm that labeling DF2 with Alexa488 does not affect liquid droplet formation. Indeed, prior to labeling DF2 with Alexa488, DF2 protein droplets were readily detectable by differential interference contrast microscopy (DIC, left). After labeling, Alexa 488-labeled DF2 protein droplets are still observed by fluorescence microscopy (right). These data indicate that the labeling protocol does not impair droplet formation by DF2. Images are taken from different protein preparations. Experiments were performed in duplicate. Scale bar, 10 μm.

c, The intrinsically disordered domain of DF2 is required for phase separation of DF2. Bright field microscopic images of recombinant DF2 lacking the N-terminal intrinsically ordered domain (YTH) and full length DF2 are shown (a schematic of the domain representation is shown above the image). The edge of the buffer (buffer-air interface) is shown with a dashed line. While the full-length YHTDF2 (75 μM) is able to phase separate, at the same concentration and in the same buffer conditions YTH cannot phase separate. This indicates that the intrinsically disordered domain is required for phase separation. Experiments were performed in duplicate. Scale bar, 10 μm.

d, DF1 and DF3 phase separate *in vitro*. Shown are fluorescence microscopy images of Alexa 594-DF1 and Alexa647-DF3. DF1 and DF3 phase separate *in vitro* as assessed by the formation of protein droplets. Experiments were performed in duplicate. Scale bar, 10 μm.

e, DF1, DF2, and DF3 form protein droplets comprising all three proteins. Shown are fluorescence microscopy images of Alexa594, 488, and 647 labeled DF1, DF2 and DF3, respectively. Mixing the three recombinant proteins shows that these proteins can phase separate together to form protein droplets containing all three proteins. Experiments were performed in duplicate. Scale bar, 10 μm.

f, Confirmation of *in vitro* transcribed RNA abundance and methylation status. *In vitro* transcribed RNAs were serially diluted (1:10) and stained for total RNA by methylene blue staining (top left panel) as well as m^{6}A abundance by immunoblotting using an anti-m^{6}A antibody (bottom left panel). RNA with no m^{6}A gave no signal while RNAs with 10 m^{6}As gave a significantly higher signal in the dot blot than those with 1 m^{6}A. Additionally, *in vitro* transcribed RNAs were analyzed on a 15% denaturing gel demonstrating the absence of degradation products (right panel). Experiments were performed in duplicate.

g, Partition coefficients of fluorescently labeled m^{6}A RNAs with and without DF2. To determine the extent to which multi-m^{6}A-RNAs were recruited into DF droplets, we synthesized a 10-m^{6}A RNAs with a 5' BODIPY FL fluorescent tag and measured its partition coefficient in the presence of DF2 (7.5 μM, 20 mM HEPES pH 7.4, 300 mM KCl, 6 mM $MgCl_2$, 0.02% NP-40, 10% glycerol). Upon addition of 850 nM BODIPY-10-m^{6}A-RNA, fluorescent RNA-containing droplets appeared in minutes (left image panel). A video of fluorescent DF2:BODIPY-10-m^{6}A-RNA coacervate droplet fusion is shown in Supplementary Video 2. Calculation of partition coefficients in comparison to background fluorescent-labeled RNAs[6] shows that m^{6}A mRNAs are enriched in DF2-containing droplets

(right graph panel; RNA only, $n = 11$; RNA+DF2, $n = 24$, where n represents distinct droplets in biological replicates). Experiment was performed in duplicate. Bar heights represent mean PCs and error bars represent SEM. ****$p < 0.0001$, two-sided Mann-Whitney test. Scale bar, 10 μm.

h, The partition coefficient of DF proteins increases over time. In this experiment we measured the partition coefficient of DF1, DF2, and DF3 as shown in Fig. 1g. However, here we measured the values after 24 h, unlike the ~5 min time point used in Fig. 1g. The partition coefficients are notably increased compared to the values measured in Fig. 1g. These suggest that droplet formation had not achieved equilibrium at the early time points used in Fig. 1g. Bar heights represent mean partition coefficients and error bars represent SEM. Experiments were performed in duplicate.

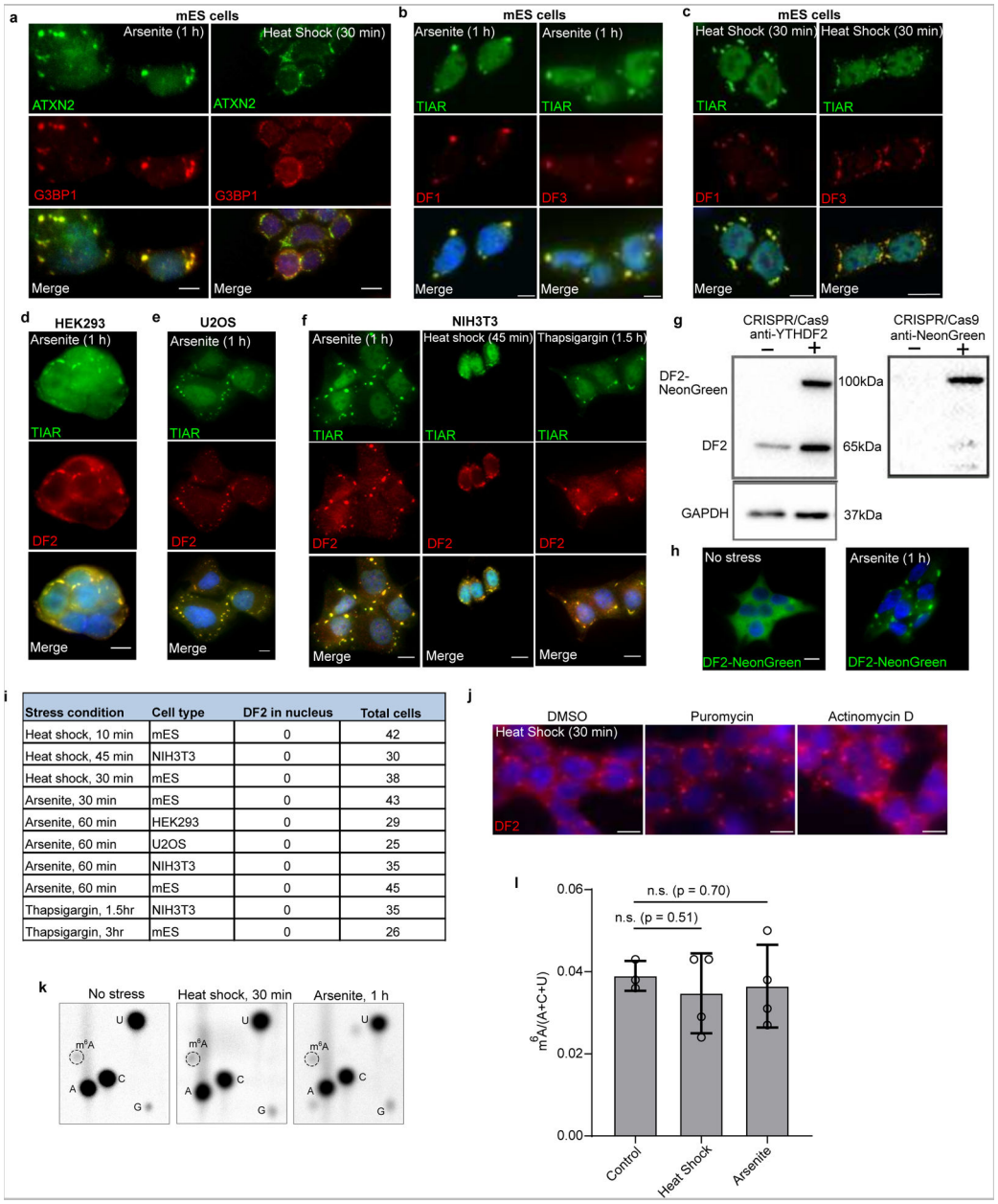

Extended Data Fig. 2. Assessing which stressors induce stress granules and the localization of DF2 proteins in diverse cell types

a, Oxidative stress and heat shock induce stress granule formation in mouse ES cells. Stress granule formation has not been extensively characterized in mouse ES cells. We therefore wanted to ensure that stress granule composition is the same in mouse ES cells compared to other cell types where stress granules are more frequently studied. To test mouse ES stress granules, we stained with additional markers. Co-immunostaining with ATXN2 (green) and G3BP1 (red) after arsenite treatment (0.5 mM for 1 h) and heat shock (42° for 30 min) in mES cells showed clear labeling of stress granules. The overlay panel shows ATXN2 and G3BP1 overlap (yellow). Thus, stress granules in mouse ES cells appear to have similar

markers as stress granules in other cell types. Experiment was performed in triplicate. Scale bar, 10μM.

b-c, DF1 and DF3 proteins relocalize to stress granules after heat shock and oxidative stress. DF1, DF2, and DF3 have high sequence similarity and show similar phase separation properties. We therefore wanted to determine if all these proteins associate with stress granules. Co-immunostaining was performed in mES cells with DF1 (red) or DF3 (red) with TIAR (green) after arsenite treatment (0.5 mM for 1 h) or heat shock (42° for 30 min). Along with DF2 shown in Fig. 2, DF1 and DF3 relocalize to stress granules treatment as visualized by the colocalization with TIAR. Scale bar, 10 μm. These findings are consistent with previous proteomic datasets of stress granules. A P-body proteome dataset[48] showed that DF2 was enriched in P-bodies. DF2 ranked 152 among 1900 P-body-associated proteins by abundance. All DF proteins were identified in a group of ~300 stress granule-enriched proteins in a proteomics study of stress granules[49]. In another study, in vivo proximity-dependent biotinylation (BioID)-labeling study of G3BP1 and other stress granule markers showed interactions with all DF proteins[50]. Another APEX labeling study[51] of G3BP1 showed that the YTHDFs are three of the top 42 G3BP1-interacting proteins in the stress granule proteome. Overall, these studies suggest that DF proteins are commonly seen in stress granules, and may be highly abundant relative to other stress granule components. Experiment was performed in triplicate.

d-f, DF2 relocalizes to stress granules after arsenite treatment in numerous cell types. The focus of this experiment was to determine if DF relocalization to stress granules is likely to be a universal feature of stress granules. We therefore tested DF localization to stress granules in multiple cell types. Shown is co-immunostaining of HEK293 cells (e), U2OS cells (f), and NIH3T3 cells (g) with DF2 (red) and TIAR (green) after arsenite treatment (0.5 mM for 1 h) and heat shock (42° for 30 min). The overlay panel shows DF2 in stress granules based on its overlap with TIAR (yellow). Experiment was performed in duplicate. Scale bar, 10 μM.

g, Confirmation of CRISPR/Cas9 knock in of DF2-NeonGreen. Western blot of HEK293T shows endogenous expression of DF2-NeonGreen.

h, Arsenite stress induces DF2-NeonGreen localization into stress granules. We wanted to determine if the ability of DF2 to phase separate *in vitro* could be actively observed in cells. Unstressed HEK293T cells expressing NeonGreen-tagged DF2 protein show a diffuse cytoplasmic fluorescent signal. Upon arsenite stress (0.5 mM, 1 h), DF2-NeonGreen phase separates into stress granules. This confirms the ability of DF2-NeonGreen to phase separate in cells in response to stress. Experiment was performed in triplicate. Scale bar, 10μm.

i, Relocalization of DF2 to the nucleus does not occur after a variety of stresses in various cell types. Because DF2 has been reported to relocalize to the nucleus 2 h after heat shock[13], we wanted to determine if any nuclear relocalization occurs in our experiments, which were performed immediately after stress. The ‘Stress condition’ column indicates the type and length of stress applied. The ‘Cell type’ column indicates the type of cell that was stressed. The ‘DF2 in nucleus’ column denotes the number of cells that were found to have DF2 in the nucleus immediately after stress. The ‘Total cells’ column indicates the number of cells that was examined for DF2 nuclear relocalization in each experimental condition. In all conditions, there was no cell that showed nuclear DF2 localization. Thus, DF2 localization is primarily in cytosolic stress granules at the time when the stress is terminated. DF2 was not

observed to relocalize to the nucleus at any time point or after any stress, including the 2 h post-heat shock conditions described previously[13].

j, DF2 relocalization to stress granules does not require new mRNA or protein synthesis. We wanted to know if an increase in DF2 expression or new m^{6}A formation could be required for stress granule formation after heat shock. To test this, we blocked protein synthesis with puromycin and blocked new transcription with actinomycin D. Actinomycin D blocks m^{6}A formation since m^{6}A formation occurs co-transcriptionally[17,18]. DF2 immunostaining in HEK293T cells treated with DMSO (left), puromycin (10 μg/mL, middle), and actinomycin D (2.5 μg/mL, right) for 15 min before and during incubation at 42°C for 30 min. The ability of DF2 to relocalize to stress granules when transcription (actinomycin D) and translation (puromycin) was arrested was assessed by immunofluorescence staining for DF2. In each case, stress granule formation was unaffected, indicating that no new protein synthesis or new methylation is required for stress granule formation. The time course of stress granule formation is rapid, making it unlikely that new protein synthesis or methylation is involved in stress granule formation. Additionally, heat shock is normally associated with inhibited transcription and translation, further suggesting that new protein synthesis and RNA methylation is unlikely to occur in the time course of stress granule formation. Based on all this data, stress granule formation likely utilizes pre-existing patterns of m^{6}A seen in unstressed cells to mediate stress granule formation. Experiment was performed in duplicate. Scale bar, 10 μm.

k-l, m^{6}A levels are not significantly altered immediately after arsenite and heat shock stress in NIH3T3 cells. We wanted to test whether m^{6}A levels in mRNA transcripts were altered as a result of cellular stress. NIH3T3 cells were subjected to arsenite (0.5 mM, 1 h) or heat shock stress (43°C, 45 min) and total RNA was extracted immediately after stress treatment. Total RNA was further purified by poly(A) selection to specifically assay m^{6}A levels in mRNA transcripts. Thin layer chromatography (TLC)[38] revealed that there was no significant increase in m^{6}A levels within poly(A) mRNA immediately after either stress condition in three biological replicates (see l). This indicates that cellular stress does not induce an increase or decrease in m^{6}A in the time frame examined. Experiments were performed in duplicate. Bar heights in l represent mean of and error bars represent SEM. Three biological replicates (n = 3) were analyzed in the control, and four biological replicates (n = 4) were analyzed after heat shock and arsenite stress. Stress m^{6}A/(A+C+U) ratios were analyzed with a two-sided student’s t-test.

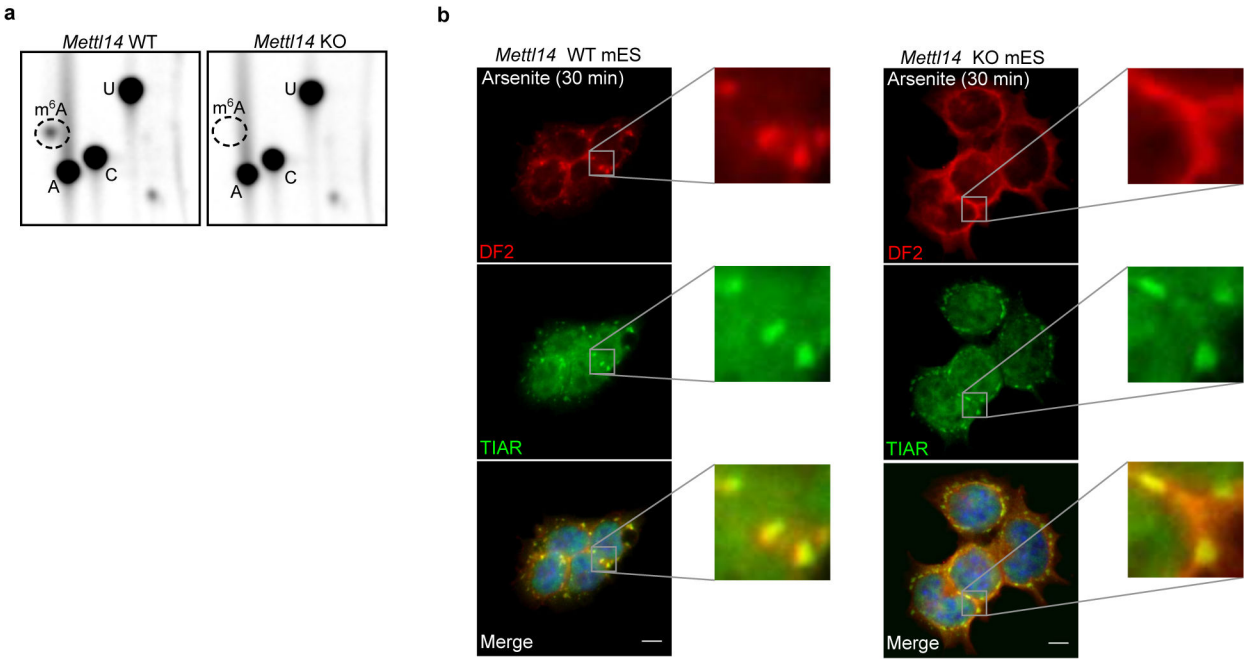

Extended Data Fig. 3. Confirmation of the *Mettl14* knockout model and DF2 phase-separation into P-bodies in mES cells

a, *Mettl14* knockout (KO) mES cells are depleted in m^{6}A RNA. We sought to independently confirm the depletion of m^{6}A from mRNA in these cells, which were previously shown to have 99% reduction in m^{6}A[19]. The TLC assay selectively quantifies m^{6}A in a G-A-C context, thereby reducing the possibility of contamination of m^{6}A from rRNA or snRNA, which are in a A-A-C or C-A-G context, respectively[38]. The protocol was performed as described previously[38]. Indicated in the TLC chromatograms is the relative position of m^{6}A (dotted circle) and adenosine (A), cytosine (C), and uracil (U). Left and the right panels show radiochromatograms obtained from 2D-TLC of poly(A) RNA from wild-type and *Mettl14* knockout cells. No m^{6}A is detectable in the poly(A) RNA derived from *Mettl14* knockout cells confirming the efficiency of m^{6}A depletion in these cells. Experiments were performed in duplicate. mES cells are used here since m^{6}A depletion can be readily achieved in *Mettl14* knockout mES cells without impairing viability[19]. In contrast, m^{6}A depletion cannot be readily achieved in immortalized cell lines as both *Mettl3* and *Mettl14* are essential for nearly all cell lines[52].

b, DF2 partitioning into stress granules induced by arsenite is impaired in m^{6}A-deficient cells. This impairment is similar to that shown in stress granules induced by heat shock as seen in Figure 3a. Experiment was performed in triplicate.

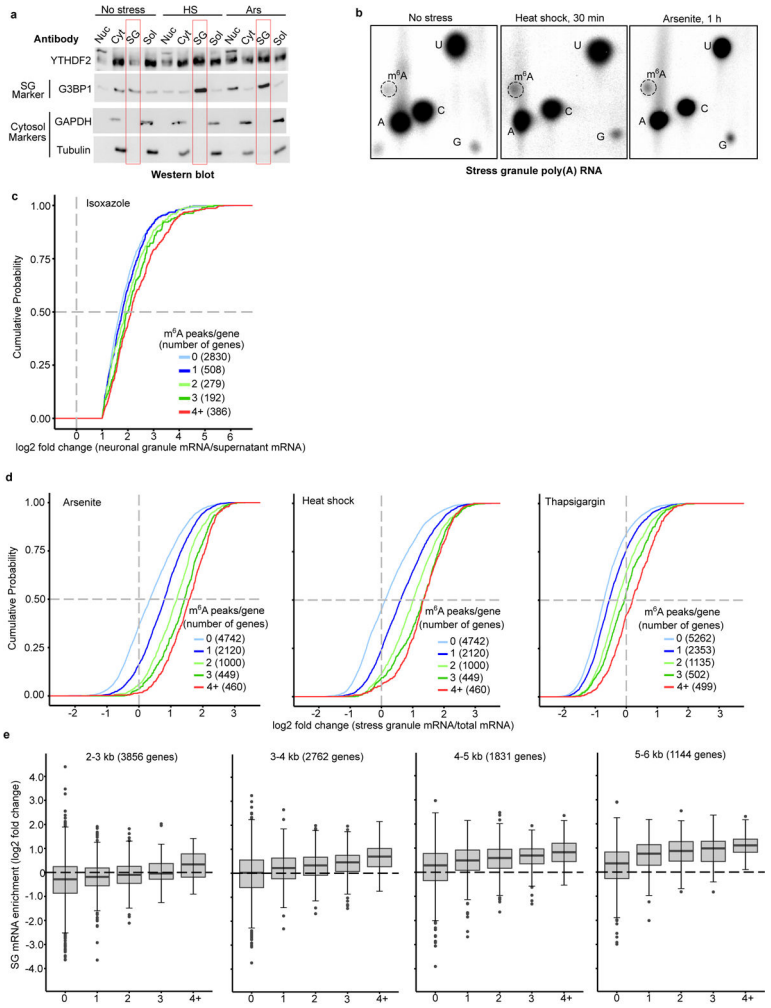

Extended Data Fig. 4. m^{6}A number is correlated with stress granule enrichment independent of transcript length

a, DF2 is enriched in stress granules after stress. Nuclear (Nuc), cytosolic (Cyt), insoluble RNA-granule enriched (SG, red boxed lanes), and soluble (Sol) protein fractions were isolated from stressed NIH3T3 cells as described previously[25]. G3BP1 was used as a stress granule marker. GAPDH and Tubulin were used as cytosolic and soluble fraction markers. Under non-stressed conditions, DF2 is most abundant in the cytoplasmic and soluble protein fractions. However, upon both arsenite and heat shock stress, the highest levels of DF2 are found in the RNA granule fraction/insoluble fraction, indicating that diverse stresses cause the partitioning of DF2 from the cytosol into stress granules. Experiment was performed in duplicate.

b, m^{6}A levels are increased in the mRNAs in the insoluble stress granule-enriched fraction after cellular stress in NIH3T3 cells. Shown are representative TLC plates analyzing m^{6}A levels in mRNAs in the stress granule fraction from the analysis presented in Fig. 4a. Representative plates from the cytosolic fraction are shown in Extended Data Fig. 2l. Experiments were performed in duplicate.

c, m^{6}A number correlates with mRNA enrichment in RNA granules in mouse neurons. In these experiments, we used mRNA enrichment data (RNA granule vs. supernatant) derived

from a study of isoxazole-induced RNA granules in mouse brain[23]. Enriched mRNAs are defined by a >1 $\log_2$ fold change in the RNA granule fraction relative to the supernatant fraction. A cumulative distribution plot of mRNA enrichment was performed for mRNAs classified by the number of called m^{6}A peaks per gene based on single-nucleotide resolution m^{6}A maps generated in mouse brain. Transcripts that contain multiple m^{6}A peaks are enriched relative in RNA granules relative to nonmethylated or singly methylated mRNAs. Original experiments were performed in triplicate.

d, The number of m^{6}A sites in an mRNA correlates with its enrichment in stress granules in NIH3T3 cells. In these experiments, we used a dataset of relative mRNA enrichment data (stress granule vs. cytoplasm) generated in a previous study[25]. Assignment of the number of m^{6}A sites in each transcript was based on a mouse embryonic fibroblast MeRIP-seq dataset obtained previously[19]. Analysis was performed as done in Fig. 4c. Polymethylated mRNAs show greater enrichment in stress granules than non-methylated or singly methylated mRNAs for each stress condition. Experiments were performed in triplicate.

e, Examination of the effect of m^{6}A on mRNA enrichment using controlled transcript size. Since transcript length positively correlates with stress granule mRNA enrichment (see refs. [24,25]), we wanted to control for this feature in our analysis. The same m^{6}A maps and RNA-Seq data from U2OS cells that were used to generate Fig. 4c were used here. Transcripts were binned based on their annotated transcript length (2–3 kb, 3–4 kb, 4–5 kb, 5–6 kb) and further sorted based on the number of annotated m^{6}A sites in each transcript. We found that mRNAs annotated with fixed lengths each showed increased enrichment based on the number of mapped m^{6}A sites. The number of m^{6}A per transcript was a positive predictor of transcript enrichment in stress granules even when controlling for transcript length. Boxplot center represents the median $\log_2$ fold change, boxplot boundaries contain genes within a quartile of the median, whiskers represent genes in the upper and lower quartiles, and outliers are presented as dots.

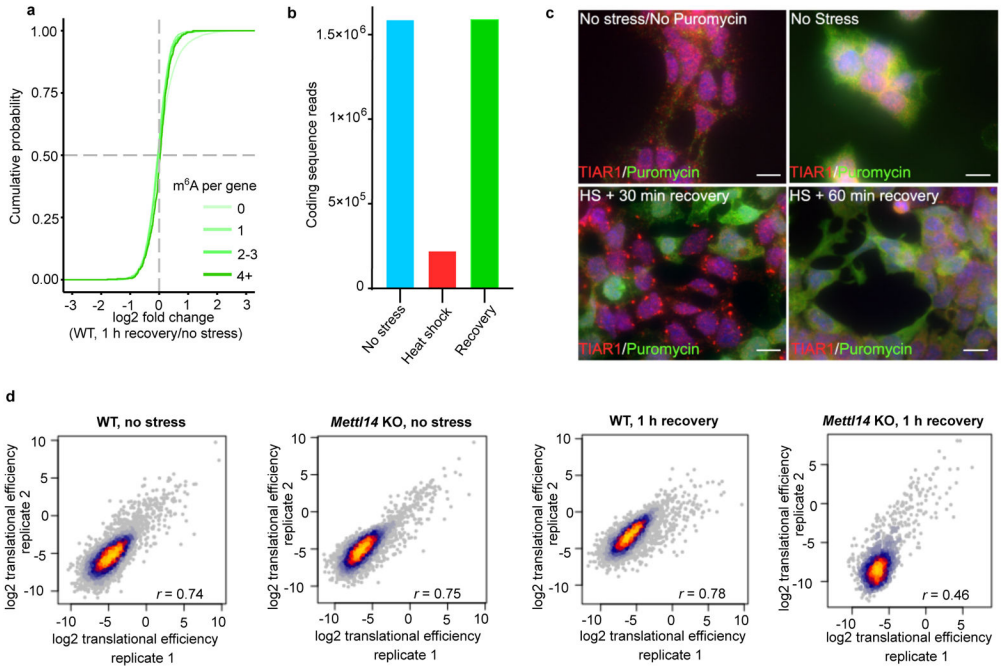

Extended Data Fig. 5. Detection of translation in mES cells after stress

a, m^6A-mRNA transcript abundance is similar before stress and after stress. We wanted to understand if mRNA transcript abundance was altered as a result of DF mobilization in mES cells after heat shock. In Extended Data Figure 5a, we examined RNA expression before heat shock and compared it to mRNA levels after 30 min of heat shock. Here, we allowed the cells to recover for 1 h, reasoning that this additional time might allow for DF-mediated mRNA degradation. As in Extended Data Figure 5a, we performed RNA-Seq on wild-type mES cells prior to heat shock and after stress, measured after cells were returned to 37ºC for 1 hour. The same m^6A annotation strategy was used as in Extended Data Figure 5a. As can be seen, the levels of m^6A in an mRNA is not correlated with an alteration in mRNA abundance. Log_2 fold change values represent the average of four biological replicates.

b, Raw counts for ribosome protected fragments. Ribosome-protected fragments were collected from mES cells before stress, immediately after heat shock (42°C, 30 min), and 1 hour after heat shock. The number of ribosome-protected fragments isolated from cells immediately following heat shock was substantially lower than the number of ribosome-protected fragments isolated before stress and 1 hour after stress. This indicates that translation is globally suppressed during the heat shock. As a result of the few ribosome-protected fragments during heat shock, translational efficiency could not be calculated during heat shock. Bar heights represent the totals from four biological replicates in each condition.

c, Translation recovers 1 h after heat shock in mES cells. Here we assessed the amount of time needed for translation to be detected after heat shock. mES cells were heat shocked for 30 min at 42°C and translation was assessed at different time points after cessation of heat shock. Translation was monitored by labeling nascent peptides with puromycin. Puromycin was added to cells for 10 min. Immunostaining with an antibody against TIAR and puromycin provides a correlation between the presence of stress granules and the translation

state. Non-stressed cells that were not treated with puromycin are shown as a control to establish the background signal (upper left). Unstressed cells treated with puromycin show robust translation (green). At a recovery time of 30 min most cells still contain stress granules (TIAR, red) and translation is absent except in the few cells lacking stress granules. However, at 1 h, translating cells can be readily detected based on puromycin immunoreactivity reactivity. Less than 50% of cells exhibit stress granules. Based on these experiments, we used 1 h as time point for our ribosome profiling experiments. Experiments were performed in duplicate. Scale bar, 10 μm.

d, Comparison of the two biological replicates with the highest percentage of CDS-mapped reads in each condition for ribosome profiling experiments. Shown are Pearson's correlation plots for the replicates used in the translational efficiency analysis shown in Fig. 4f and 4g.

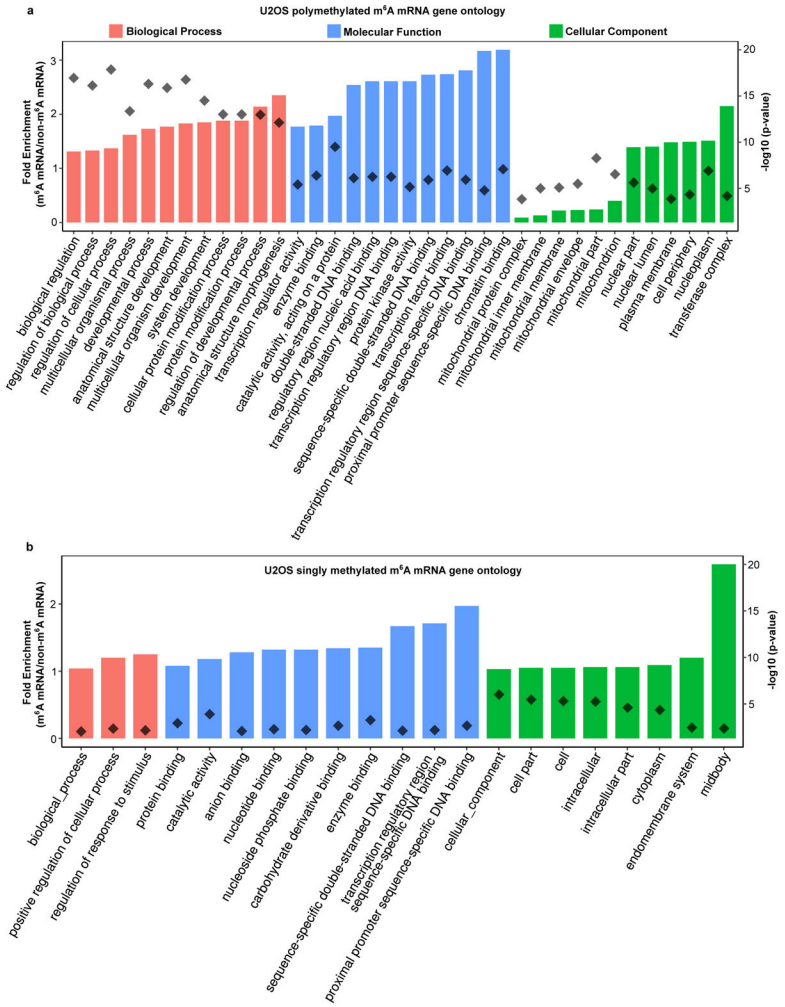

Extended Data Fig. 6. Gene ontology of polymethylated and singly methylated mRNAs in U2OS cells.

a-b, Gene ontology of m^{6}A-mRNAs in U2OS cells. U2OS RNA-seq data from Khong, et al. [24] and Me-RIP-seq data from Xiang et al.[32] was used in a gene ontology analysis for polymethylated m^{6}A-mRNAs in U2OS cells. Polymethylated mRNAs were defined as all mRNAs having four or more annotated m^{6}A sites in the MeRIP-seq dataset that were identified in the U2OS RNA-seq (n = 652). Singly methylated mRNAs were defined as mRNAs having one annotated m^{6}A site with the same criteria (n = 2896). Gene ontology was performed using the PANTHER gene ontology (GO) database. The biological process GO search showed enrichment of regulatory and developmental-associated genes in the polymethylated group. The molecular function GO search showed enrichment of protein, ion, enzyme, and adenylyl-binding proteins, and de-enrichment of ribosome structural components. The cellular component GO search showed de-enrichment of mitochondrial and ribosomal proteins, and enrichment of components of the nucleus and cell membrane. mRNAs that met the same inclusion criteria but had zero annotated m^{6}A sites were used as the reference category for the GO analysis (n = 5956). Fold enrichment scores for each GO category are indicated by the colored bars and correspond to the left y-axis. P-values for each GO category are indicated by the dark grey diamonds and correspond to the right y-

axis. P-values were determined with Fisher's exact test and a Bonferroni correction was performed for multiple hypothesis testing.

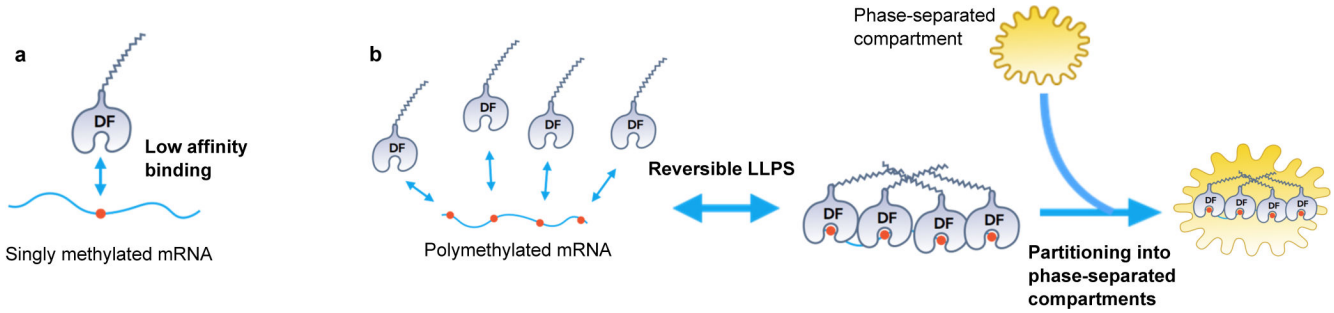

Extended Data Fig. 7. Model of how the properties of m^{6}A-containing mRNAs are determined by their phase separation into intracellular phase-separated compartments

a, Depicted is the binding of DF proteins to singly methylated mRNAs. DF proteins show low affinity interactions with m^{6}A containing mRNAs. Affinities typically range between 0.9–1.1 μM for DF1, DF2, and DF3[4,36]. These low affinities suggest that DF proteins would not be able to form a stable bimolecular interaction with singly methylated RNA. The low affinity can now be understood in the context of phase separation. Their weak interactions with RNA are likely stabilized by interactions between their low-complexity domains, and subsequent phase separation. Notably, all m^{6}A sites in cytosolic mRNAs appear to have an equal propensity to bind each DF protein[35]. Thus, any m^{6}A residue may be sufficient to enhance the phase-separation potential of an mRNA. However, higher-level information, such as the spacing of m^{6}A sites, as well as other mRNA-bound proteins with low-complexity domains, may affect the efficiency of phase separation.

b, Polymethylated mRNAs bind multiple DF proteins leading to phase separation. When multiple DF proteins bind to a polymethylated mRNA, their interactions with the mRNA are stabilized by DF-DF interactions mediated by their low-complexity domains. These complexes may be reversible and undergo an assembly/disassembly equilibrium. However, if P-bodies, neuronal granules or stress granules are present, the DF-mRNA complexes can partition into these structures. m^{6}A-mRNA is then regulated by the regulatory proteins and functional properties of these distinct structures. If an mRNA has a single m^{6}A site, the mRNA can still partition into phase-separated structures, especially if RNA-RNA interactions or other RNA-protein interactions can facilitate phase separation. The DF low-complexity domain could interact with these non-DF proteins to enhance mRNA partitioning. Overall, interactions between DF proteins and m^{6}A mRNAs probably lower the saturation concentration for their incorporation within stress granules, enhancing their partitioning over non-methylated mRNAs

Supplementary Material

Refer to Web version on PubMed Central for supplementary material.

Acknowledgments

We thank members of the Jaffrey laboratory for comments and suggestions, members of the Epigenomics, Optical Microscopy & Imaging and Flow Cytometry Weill Cornell Cores for their assistance. We thank J. Hanna and S. Geula for generously providing *Mettl14* knockout and control mES lines. This work was supported by NIH grants R01DA037755 (S.R.J.), F32CA22104–01 (B.F.P), R01DK114131 (J.H.L.), T32CA062948 (A.-O.G.), and an American-Italian Cancer Foundation fellowship (S.Z.).

REFERENCES

1. Perry RP & Kelley DE Existence of methylated messenger RNA in mouse L cells. Cell 1, 37–42 (1974).
2. Desrosiers R, Friderici K & Rottman F Identification of methylated nucleosides in messenger RNA from Novikoff hepatoma cells. Proc Natl Acad Sci U S A 71, 3971–3975 (1974). [PubMed: 4372599]
3. Meyer KD & Jaffrey SR Rethinking m^{6}A Readers, Writers, and Erasers. Annu Rev Cell Dev Biol 33, 319–342 (2017). [PubMed: 28759256]
4. Patil DP, Pickering BF & Jaffrey SR Reading m(6)A in the Transcriptome: m(6)A-Binding Proteins. Trends Cell Biol (2017).
5. Nott TJ, Petsalaki E, Farber P, Jervis D, Fussner E, Plochowietz A, Craggs TD, Bazett-Jones DP, Pawson T, Forman-Kay JD & Baldwin AJ Phase transition of a disordered nuage protein generates environmentally responsive membraneless organelles. Mol Cell 57, 936–947 (2015). [PubMed: 25747659]
6. Lin Y, Protter DS, Rosen MK & Parker R Formation and Maturation of Phase-Separated Liquid Droplets by RNA-Binding Proteins. Mol Cell 60, 208–219 (2015). [PubMed: 26412307]
7. Quiroz FG & Chilkoti A Sequence heuristics to encode phase behaviour in intrinsically disordered protein polymers. Nat Mater 14, 1164–1171 (2015). [PubMed: 26390327]
8. Wisniewski JR, Hein MY, Cox J & Mann MA “proteomic ruler” for protein copy number and concentration estimation without spike-in standards. Mol Cell Proteomics 13, 3497–3506 (2014). [PubMed: 25225357]
9. Shin Y & Brangwynne CP Liquid phase condensation in cell physiology and disease. Science 357 (2017).
10. Molliex A, Temirov J, Lee J, Coughlin M, Kanagaraj AP, Kim HJ, Mittag T & Taylor JP Phase separation by low complexity domains promotes stress granule assembly and drives pathological fibrillization. Cell 163, 123–133 (2015). [PubMed: 26406374]
11. Kroschwald S, Maharana S, Mateju D, Malinovska L, Nuske E, Poser I, Richter D & Alberti S Promiscuous interactions and protein disaggregases determine the material state of stress-inducible RNP granules. Elife 4, e06807 (2015). [PubMed: 26238190]
12. Standart N & Weil D P-Bodies: Cytosolic Droplets for Coordinated mRNA Storage. Trends Genet 34, 612–626 (2018). [PubMed: 29908710]
13. Zhou J, Wan J, Gao X, Zhang X, Jaffrey SR & Qian SB Dynamic m^{6}A mRNA methylation directs translational control of heat shock response. Nature 526, 591–594 (2015). [PubMed: 26458103]
14. Dominissini D, Moshitch-Moshkovitz S, Schwartz S, Salmon-Divon M, Ungar L, Osenberg S, Cesarkas K, Jacob-Hirsch J, Amariglio N, Kupiec M, Sorek R & Rechavi G Topology of the human and mouse m^{6}A RNA methylomes revealed by m^{6}A-seq. Nature 485, 201–206 (2012). [PubMed: 22575960]
15. Meyer KD, Patil DP, Zhou J, Zinoviev A, Skabkin MA, Elemento O, Pestova TV, Qian SB & Jaffrey SR 5’ UTR m^{6}A Promotes Cap-Independent Translation. Cell 163, 999–1010 (2015). [PubMed: 26593424]
16. Anders M, Chelysheva I, Goebel I, Trenkner T, Zhou J, Mao Y, Verzini S, Qian S-B & Ignatova Z Dynamic m^{6}A methylation facilitates mRNA triaging to stress granules. Life Science Alliance 1, e201800113 (2018). [PubMed: 30456371]
17. Slobodin B, Han R, Calderone V, Vrielink JA, Loayza-Puch F, Elkon R & Agami R Transcription Impacts the Efficiency of mRNA Translation via Co-transcriptional N6-adenosine Methylation. Cell 169, 326–337 e312 (2017). [PubMed: 28388414]
18. Knuckles P, Carl SH, Musheev M, Niehrs C, Wenger A & Buhler M RNA fate determination through cotranscriptional adenosine methylation and microprocessor binding. Nat Struct Mol Biol 24, 561–569 (2017). [PubMed: 28581511]
19. Geula S, Moshitch-Moshkovitz S, Dominissini D, Mansour AA, Kol N, Salmon-Divon M, Hershkovitz V, Peer E, Mor N, Manor YS, Ben-Haim MS, Eyal E, Yunger S, Pinto Y, Jaitin DA, Viukov S, Rais Y, Krupalnik V, Chomsky E, Zerbib M, Maza I, Rechavi Y, Massarwa R, Hanna S, Amit I, Levanon EY, Amariglio N, Stern-Ginossar N, Novershtern N, Rechavi G & Hanna JH

Stem cells. m^{6}A mRNA methylation facilitates resolution of naive pluripotency toward differentiation. Science 347, 1002–1006 (2015). [PubMed: 25569111]

20. Wang P, Doxtader KA & Nam Y Structural Basis for Cooperative Function of Mettl3 and Mettl14 Methyltransferases. Mol Cell 63, 306–317 (2016). [PubMed: 27373337]
21. Wang X, Feng J, Xue Y, Guan Z, Zhang D, Liu Z, Gong Z, Wang Q, Huang J, Tang C, Zou T & Yin P Structural basis of N^6-adenosine methylation by the METTL3-METTL14 complex. Nature 534, 575–578 (2016). [PubMed: 27281194]
22. Sledz P & Jinek M Structural insights into the molecular mechanism of the m(6)A writer complex. Elife 5 (2016).
23. Han TW, Kato M, Xie S, Wu LC, Mirzaei H, Pei J, Chen M, Xie Y, Allen J, Xiao G & McKnight SL Cell-free formation of RNA granules: bound RNAs identify features and components of cellular assemblies. Cell 149, 768–779 (2012). [PubMed: 22579282]
24. Khong A, Matheny T, Jain S, Mitchell SF, Wheeler JR & Parker R The Stress Granule Transcriptome Reveals Principles of mRNA Accumulation in Stress Granules. Mol Cell 68, 808–820 e805 (2017). [PubMed: 29129640]
25. Namkoong S, Ho A, Woo YM, Kwak H & Lee JH Systematic Characterization of Stress-Induced RNA Granulation. Mol Cell 70, 175–187 e178 (2018). [PubMed: 29576526]
26. Wang X, Lu Z, Gomez A, Hon GC, Yue Y, Han D, Fu Y, Parisien M, Dai Q, Jia G, Ren B, Pan T & He C N^6-methyladenosine-dependent regulation of messenger RNA stability. Nature 505, 117–120 (2014). [PubMed: 24284625]
27. Bouche G, Amalric F, Caizergues-Ferrer M & Zalta JP Effects of heat shock on gene expression and subcellular protein distribution in Chinese hamster ovary cells. Nucleic Acids Res 7, 1739–1747 (1979). [PubMed: 537909]
28. Van Treeck B & Parker R Emerging Roles for Intermolecular RNA-RNA Interactions in RNP Assemblies. Cell 174, 791–802 (2018). [PubMed: 30096311]
29. Meyer KD, Saletore Y, Zumbo P, Elemento O, Mason CE & Jaffrey SR Comprehensive analysis of mRNA methylation reveals enrichment in 3' UTRs and near stop codons. Cell 149, 1635–1646 (2012). [PubMed: 22608085]
30. Kedersha N, Stoecklin G, Ayodele M, Yacono P, Lykke-Andersen J, Fritzler MJ, Scheuner D, Kaufman RJ, Golan DE & Anderson P Stress granules and processing bodies are dynamically linked sites of mRNP remodeling. J Cell Biol 169, 871–884 (2005). [PubMed: 15967811]
31. Zhu T, Roundtree IA, Wang P, Wang X, Wang L, Sun C, Tian Y, Li J, He C & Xu Y Crystal structure of the YTH domain of YTHDF2 reveals mechanism for recognition of N^6-methyladenosine. Cell Res 24, 1493–1496 (2014). [PubMed: 25412661]
32. Xiang Y, Laurent B, Hsu CH, Nachtergaele S, Lu Z, Sheng W, Xu C, Chen H, Ouyang J, Wang S, Ling D, Hsu PH, Zou L, Jambhekar A, He C & Shi Y RNA m^{6}A methylation regulates the ultraviolet-induced DNA damage response. Nature 543, 573–576 (2017). [PubMed: 28297716]
33. Knuckles P, Lence T, Haussmann IU, Jacob D, Kreim N, Carl SH, Masiello I, Hares T, Villasenor R, Hess D, Andrade-Navarro MA, Biggiogera M, Helm M, Soller M, Buhler M & Roignant JY Zc3h13/Flacc is required for adenosine methylation by bridging the mRNA-binding factor Rbm15/Spenito to the m(6)A machinery component Wtap/Fl(2)d. Genes Dev 32, 415–429 (2018). [PubMed: 29535189]
34. Wen J, Lv R, Ma H, Shen H, He C, Wang J, Jiao F, Liu H, Yang P, Tan L, Lan F, Shi YG, He C, Shi Y & Diao J Zc3h13 Regulates Nuclear RNA m(6)A Methylation and Mouse Embryonic Stem Cell Self-Renewal. Mol Cell 69, 1028–1038 e1026 (2018). [PubMed: 29547716]
35. Patil DP, Chen CK, Pickering BF, Chow A, Jackson C, Guttman M & Jaffrey SR m^{6}A RNA methylation promotes XIST-mediated transcriptional repression. Nature 537, 369–373 (2016). [PubMed: 27602518]
36. Xu C, Liu K, Ahmed H, Loppnau P, Schapira M & Min J Structural Basis for the Discriminative Recognition of N6-Methyladenosine RNA by the Human YT521-B Homology Domain Family of Proteins. J Biol Chem 290, 24902–24913 (2015). [PubMed: 26318451]
37. Zhang H, Elbaum-Garfinkle S, Langdon EM, Taylor N, Occhipinti P, Bridges AA, Brangwynne CP & Gladfelter AS RNA Controls PolyQ Protein Phase Transitions. Mol Cell 60, 220–230 (2015). [PubMed: 26474065]

38. Zhong S, Li H, Bodi Z, Button J, Vespa L, Herzog M & Fray RG MTA is an Arabidopsis messenger RNA adenosine methylase and interacts with a homolog of a sex-specific splicing factor. Plant Cell 20, 1278–1288 (2008). [PubMed: 18505803]
39. Hoover DM & Lubkowski J DNAWorks: an automated method for designing oligonucleotides for PCR-based gene synthesis. Nucleic Acids Res 30, e43 (2002). [PubMed: 12000848]
40. Li H, Beckman KA, Pessino V, Huang B, Weissman JS & Leonetti MD Design and specificity of long ssDNA donors for CRISPR-based knock-in. bioRxiv, 178905 (2017).
41. Linder B, Grozhik AV, Olarerin-George AO, Meydan C, Mason CE & Jaffrey SR Single-nucleotide-resolution mapping of m^6A and m^6Am throughout the transcriptome. Nat Methods 12, 767–772 (2015). [PubMed: 26121403]
42. Dobin A, Davis CA, Schlesinger F, Drenkow J, Zaleski C, Jha S, Batut P, Chaisson M & Gingeras TR STAR: ultrafast universal RNA-seq aligner. Bioinformatics 29, 15–21 (2013). [PubMed: 23104886]
43. McGlincy NJ & Ingolia NT Transcriptome-wide measurement of translation by ribosome profiling. Methods 126, 112–129 (2017). [PubMed: 28579404]
44. Xiao Z, Zou Q, Liu Y & Yang X Genome-wide assessment of differential translations with ribosome profiling data. Nat Commun 7, 11194 (2016). [PubMed: 27041671]
45. Mi H, Dong Q, Muruganujan A, Gaudet P, Lewis S & Thomas PD PANTHER version 7: improved phylogenetic trees, orthologs and collaboration with the Gene Ontology Consortium. Nucleic Acids Res 38, D204–210 (2010). [PubMed: 20015972]
46. Lancaster AK, Nutter-Upham A, Lindquist S & King OD PLAAC: a web and command-line application to identify proteins with prion-like amino acid composition. Bioinformatics 30, 2501–2502 (2014). [PubMed: 24825614]
47. Gilles JF, Dos Santos M, Boudier T, Bolte S & Heck N DiAna, an ImageJ tool for object-based 3D co-localization and distance analysis. Methods 115, 55–64 (2017). [PubMed: 27890650]
48. Hubstenberger A, Courel M, Benard M, Souquere S, Ernoult-Lange M, Chouaib R, Yi Z, Morlot JB, Munier A, Fradet M, Daunesse M, Bertrand E, Pierron G, Mozziconacci J, Kress M & Weil D P-Body Purification Reveals the Condensation of Repressed mRNA Regulons. Mol Cell 68, 144–157 e145 (2017). [PubMed: 28965817]
49. Jain S, Wheeler JR, Walters RW, Agrawal A, Barsic A & Parker R ATPase-Modulated Stress Granules Contain a Diverse Proteome and Substructure. Cell 164, 487–498 (2016). [PubMed: 26777405]
50. Youn JY, Dunham WH, Hong SJ, Knight JDR, Bashkurov M, Chen GI, Bagci H, Rathod B, MacLeod G, Eng SWM, Angers S, Morris Q, Fabian M, Cote JF & Gingras AC High-Density Proximity Mapping Reveals the Subcellular Organization of mRNA-Associated Granules and Bodies. Mol Cell 69, 517–532 e511 (2018). [PubMed: 29395067]
51. Markmiller S, Soltanieh S, Server KL, Mak R, Jin W, Fang MY, Luo EC, Krach F, Yang D, Sen A, Fulzele A, Wozniak JM, Gonzalez DJ, Kankel MW, Gao FB, Bennett EJ, Lecuyer E & Yeo GW Context-Dependent and Disease-Specific Diversity in Protein Interactions within Stress Granules. Cell 172, 590–604 e513 (2018). [PubMed: 29373831]
52. Tsherniak A, Vazquez F, Montgomery PG, Weir BA, Kryukov G, Cowley GS, Gill S, Harrington WF, Pantel S, Krill-Burger JM, Meyers RM, Ali L, Goodale A, Lee Y, Jiang G, Hsiao J, Gerath WFJ, Howell S, Merkel E, Ghandi M, Garraway LA, Root DE, Golub TR, Boehm JS & Hahn WC Defining a Cancer Dependency Map. Cell 170, 564–576 e516 (2017). [PubMed: 28753430]

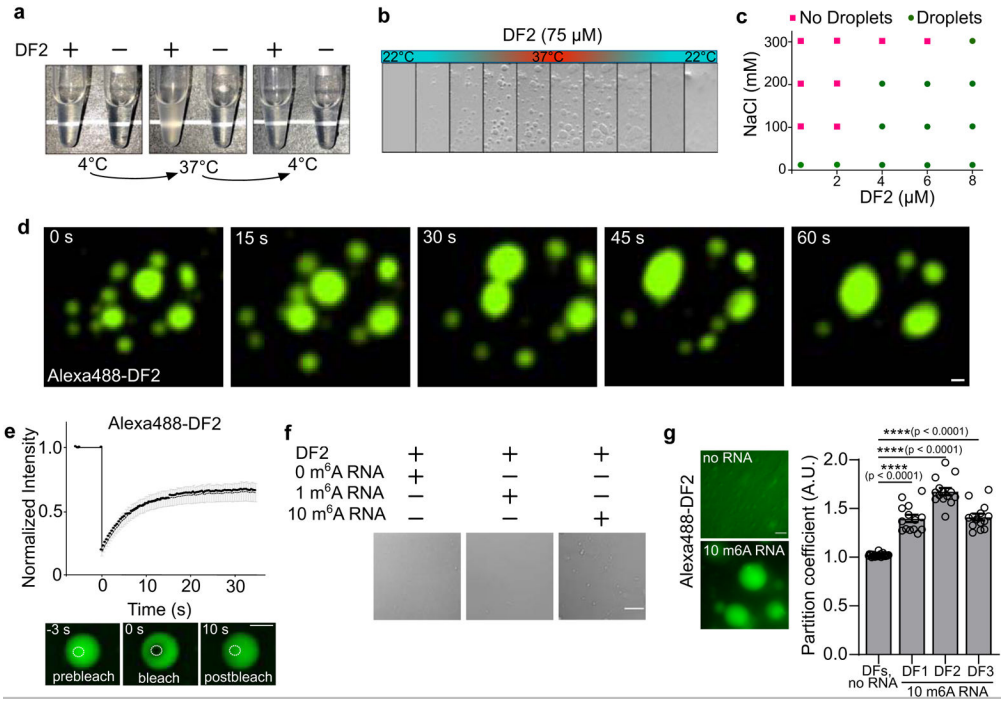

Fig. 1. Polymethylated m^{6}A RNAs trigger liquid-liquid phase separation of DF proteins

a, Tubes containing either buffer only or recombinant DF2 (75 μM, 20 mM HEPES pH 7.4, 300 mM KCl, 6 mM $MgCl_2$, 0.02% NP-40) were heated from 4°C to 37°C. DF2 phase separates when heated; this is reversible upon cooling.

b, Time-lapse of bright field microscopy images of DF2 droplets (75 μM) subjected to temperature gradient. Temperature was increased (1°C per minute) from 22°C to 37°C enabling the formation of protein droplets. Lowering the temperature back to 22°C causes disassembly.

c, Phase diagram of DF2 in the presence of different concentrations of NaCl (0, 100, 200, and 300 mM) showing salt dampens its phase separation potential. Green circles: protein droplets present; pink squares, no protein droplets observed in the buffer.

d, Alexa488-DF2 (75 μM) was imaged by fluorescent microscopy over 1 min. A video of Alexa488-DF2 droplet fusion can be seen in Supplementary Video 1. Scale bar, 10 μm.

e, Changes in Alexa488-DF2 droplet fluorescence intensity after photobleaching were plotted over time (top panel). Background was subtracted from the fluorescence measurement. The black curve represents the mean of the fluorescence intensity in the photobleached region of interest in distinct droplets (n = 8). The grey bars indicate SEM. Representative images of fluorescence recovery are shown in the bottom panel. Scale bar, 10 μm.

f, A 65-nt RNA containing 10 m^{6}As (570 nM) induces DF2 (25 μM) to rapidly form small liquid droplets, while RNA containing 1 m^{6}A or 0 m^{6}A, does not cause significant DF2 phase separation. Scale bar, 10 μm.

g, Adding RNA containing 10 m^{6}A sites (425 nM) enhances the phase separation of DFs (15 μM) in solution (bottom left panel). For the no RNA condition, partition coefficients (PC) were calculated immediately before the addition of m^{6}A-containing RNA (right panel; DFs, no RNA mean PC = 1.0; DF1, n = 8; DF2, n = 10; DF3, n = 9; total n = 27. Partition

coefficients for the DFs were measured shortly after the addition of ten m^6A RNAs and mean DF PCs increased measurably (right panel; DF1 mean PC = 1.40, $n = 14$; DF2 mean PC = 1.67, $n = 14$; DF3 mean PC = 1.41, $n = 14$ droplets) within minutes of adding 10 m^6A RNA. Error bars represent SEM. n represents the number of droplets from technical replicates. Two-sided Mann-Whitney test. Scale bar, 10 μm.

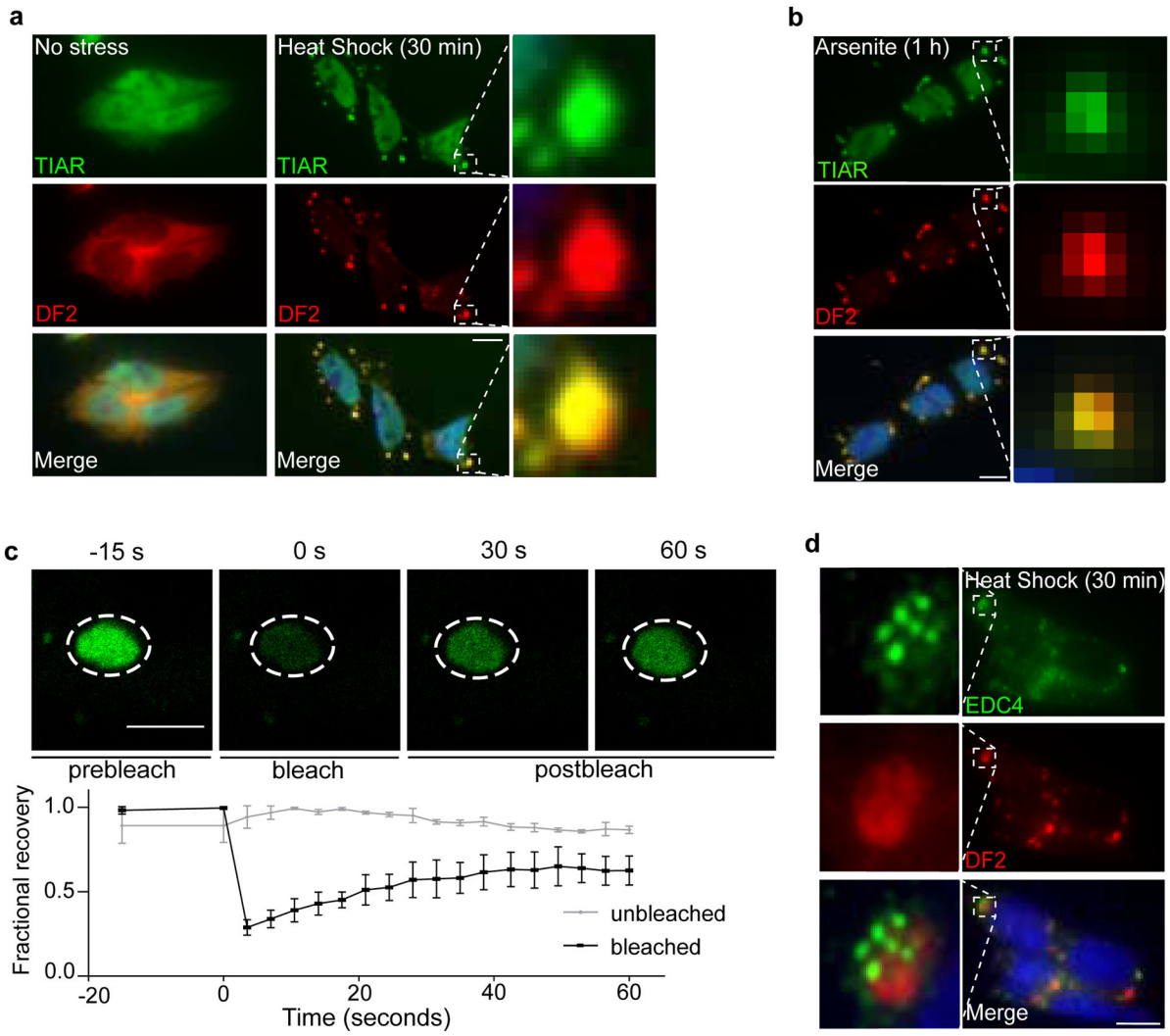

Fig. 2. DF proteins exhibit liquid-like properties in cells and relocalize during stress

a-b, Co-immunostaining of DF2 (red) and the stress granule marker TIAR (green) in mouse embryonic stem cells (mES) before and after incubation at 42°C for 30 min (a) or treatment with sodium arsenite (0.5 mM) for 1 hr (b). DF2 relocalizes to stress granules as visualized by its colocalization with TIAR (yellow) in the overlay panel (bottom). Scale bar, 10 μm.

c, DF2-NeonGreen was endogenously expressed in HEK293 cells using CRISPR/Cas9 knock-in and treated with arsenite (0.5 mM, 1 h). DF2-NeonGreen partitioned into arsenite-induced stress granules. Photobleaching of stress granules is followed by rapid recovery of fluorescence, indicating that DF2-NeonGreen can actively phase separate in cells. The line traces represent mean fractional fluorescence (unbleached $n = 3$; bleached $n = 3$). Error bars represent SEM. Scale bar, 5 μm.

d, P-bodies have been shown to be adjacent to stress granules[30]. We observed the proximity between P-bodies and stress granules by co-immunostaining of the stress granule marker DF2 (red) and the P-body marker EDC4 (green) in mES cells after heat shock stress (42°C, 30 min). DF2-labeled stress granules and P-bodies are in close proximity but do not colocalize. Scale bar, 10 μm.

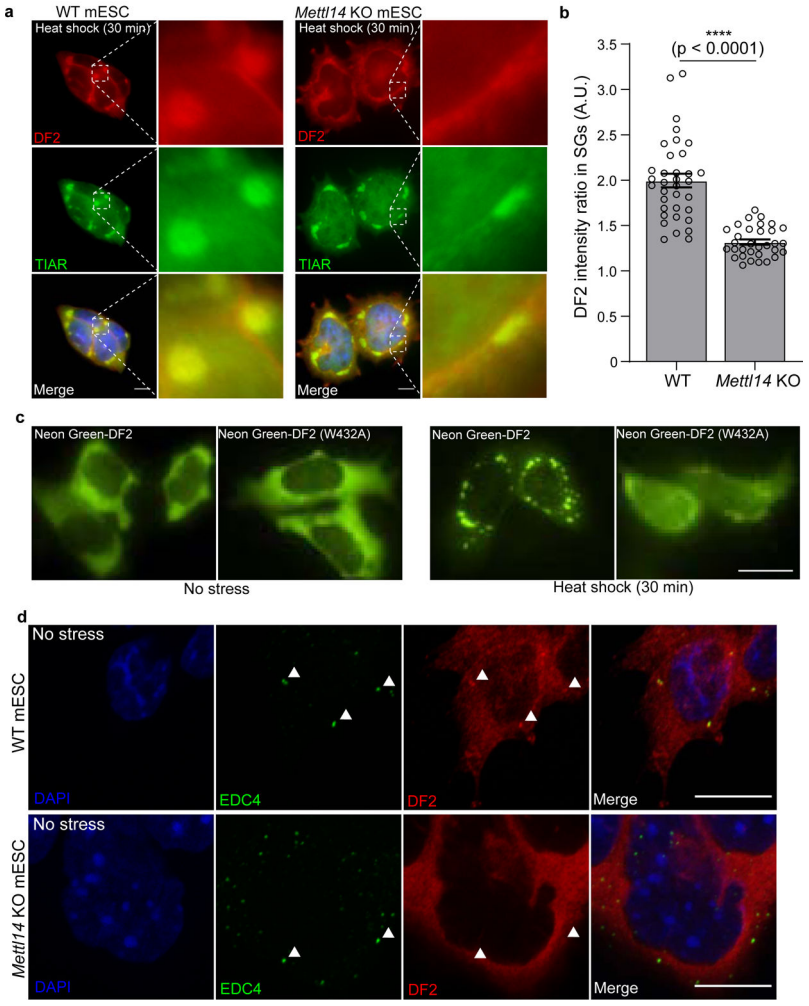

Fig. 3. m^{6}A enhances the ability of DF proteins to partition into intracellular phase-separated compartments

a, Stress granules form normally in both in wild-type and *Mettl14* knockout mES cells, which lack m^{6}A-mRNA, but DF2 relocalization in *Mettl14* knockout mES cells is delayed. Co-immunostaining was performed using the stress granule marker TIAR (green) and DF2 (red) after heat shock (42°C, 30 min) or arsenite stress (0.5 mM, 30 min). Scale bar, 10 μm.

b, DF2 fluorescence intensity ratios in stress granules (DF2 intensity inside TIAR-stained granules vs. DF2 intensity in the cytoplasm immediately adjacent to TIAR-stained granules) in wild type and *Mettl14* knockout mES cells (WT, $n = 35$; *Mettl14* knockout, $n = 32$) shows delayed DF2 co-localization in *Mettl14* knockout cells. n represents stress granules from biological replicates. Bar height represents mean fluorescence intensity ratios and error bars represent SEM. Two-sided Mann-Whitney test.

c, The localization of a DF2 mutant with ~10-fold reduced affinity for m^{6}A (W432A)[31] to stress granules is impaired after heat shock (42°C, 30 min). The W432A mutation disrupts the m^{6}A-binding tryptophan cage in DF2[31]. Plasmids expressing NeonGreen-tagged DF2 and NeonGreen-tagged DF2 W432A were transfected into wild-type mES cells and images were taken before (left panels) and after (right panels) heat shock (42°C, 30 min). Scale bar, 10 μm.

d, Co-immunostaining showed well-defined overlap between DF2 (red) and P-bodies as labeled by EDC4 (green) in wild-type mES cells. However, in *Mettl14* knockout cells, this co-localization was markedly reduced and DF2 appeared more diffusely cytosolic. Representative images from slices of a confocal Z-stack are shown. Individual P-bodies and their region of overlap with DF2 are indicated by white arrowheads. Scale bar, 10 μm.

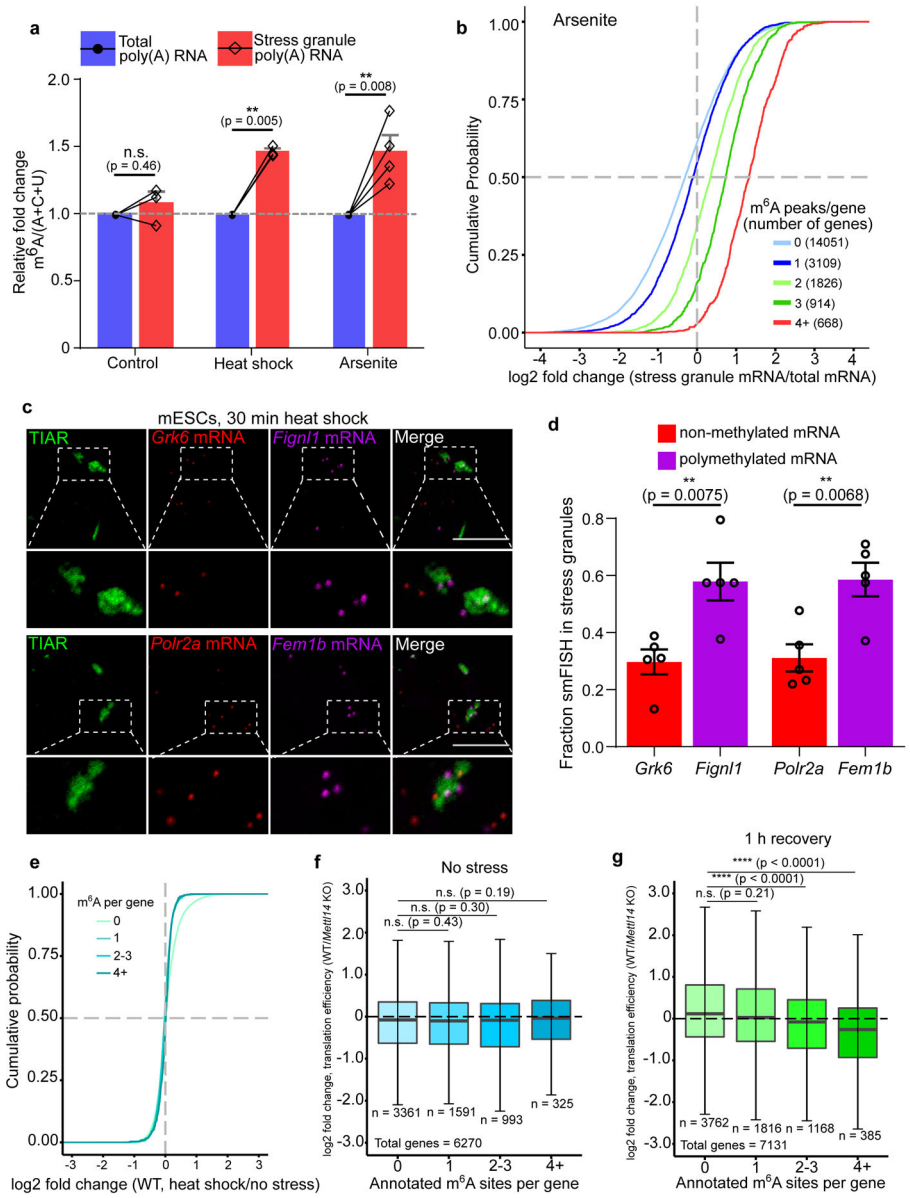

Fig. 4. m^{6}A-containing mRNAs are enriched in distinct DF-containing RNA granules.

a, m^{6}A levels were measured in poly(A) RNA purified from the insoluble stress granule-enriched fraction and poly(A) RNA prepared from total NIH3T3 cellular extracts. m^{6}A levels were quantified by TLC, and normalized to the combined intensities of A, C, and U. In non-stressed cells, there was no significant difference in the level of m^{6}A-mRNA in the total cellular or insoluble RNA fraction. In contrast, a significant increase in m^{6}A levels was detected in the stress granule fraction obtained from either heat shocked or arsenite stressed cells (control, $n = 3$; heat shock, $n = 4$; arsenite $n = 4$, where n represent biological replicates). Bar heights represent mean normalized fold change of m^{6}A/(A+C+U) in poly(A) RNA from stress granules over poly(A) RNA from total cellular RNA (control = 107.6, heat shock = 149, arsenite = 150.3). Filled circles and diamonds with lines represent paired

biological samples. Error bars represent SEM. Paired two-sided student's t-test performed on unnormalized $m^6A/(A+C+U)$ fractions between control and stress conditions.

b, A cumulative distribution plot of mRNA enrichment in U2OS arsenite-induced stress granules[24] was plotted for mRNAs classified by the number of annotated m^6A peaks[32] per transcript. Transcripts with 0 m^6A peaks (i.e., non-methylated) are slightly depleted in stress granules relative to total cellular RNA. However, transcripts that contain 2 or more m^6A peaks show enrichment in stress granules in proportion to the number of m^6A sites.

c-d, m^6A-containing mRNAs show higher enrichment in stress granules compared to non-methylated mRNAs using smFISH. Two mRNAs that lack any annotated m^6A sites (*Grk6* and *Polr2a*) were matched with m^6A-containing mRNAs of similar length and abundance (*Fignl1* and *Fem1b*, four m^6A sites each[19]). *Grk6* and *Polr2a* are not enriched in stress granules (d). *Fignl1* and *Fem1b* are markedly more enriched within stress granules as a fraction of total smFISH puncta after heat shock stress. In c, representative slices from confocal Z-stacks are shown to demonstrate localization. In d, images (*Grk6/Fignl1* $n = 5$ images, 26 cells, 2 biological replicates; *Polr2a/Fem1b* $n = 5$ images, 24 cells, 2 biological replicates) were analyzed to assess mRNA localization to stress granules. Bar heights represent mean fraction of stress granule-localized smFISH puncta and error bars represent SEM. Two-sided student's t-test.

e, mRNA expression levels were determined by RNA-seq before and after heat shock (42°C, 30 min). Transcript abundance was unaltered for non-methylated, singly methylated, and polymethylated m^6A-mRNAs.

f, Translation efficiency prior to heat shock was calculated using matched ribosome profiling and RNA-seq data and compared for each mRNA in the methylated state (i.e., in wild-type cells) versus the nonmethylated state (i.e., in *Mettl14* knockout cells). Transcripts were binned based on the annotated number of m^6A sites as in e. Boxplot center represents the median $\log_2$ fold change, boxplot boundaries contain genes within a quartile of the median, and whiskers represent genes in the upper and lower quartiles. m^6A-mRNAs in wild type mES cells did not display a significant difference in translational efficiency compared to *Mettl14* knockout mES cells. *n* denotes the number of genes in each bin. Binned gene groups with annotated m^6A sites were compared to genes with no m^6A sites with an unpaired two-sided student's t-test.

g, Translation efficiency in wild-type and *Mettl14* knockout mES cells subjected to 30 min of continuous heat followed by 1 hr recovery at 37°C. Only polymethylated transcripts showed significantly decreased translation efficiency. The effect of m^6A is determined by comparing the translation efficiency for each transcript in the methylated form (wild-type cells) relative to the same transcript in the nonmethylated form (*Mettl14* knockout cells). The same binning and m^6A annotation strategy were employed as in f. Boxplots are presented as in f. *n* denotes the number of genes in each bin. Binned gene groups with annotated m^6A sites were compared to genes with no m^6A sites with an unpaired two-sided student's t-test.